CZECH TECHNICAL UNIVERSITY IN PRAGUE

FACULTY OF BIOMEDICAL ENGINEERING

Department of Biomedical Technology

A Phantom Feasibility Study of Differential Microwave Temperature Monitoring of Regional Hyperthermia

Bachelor's Thesis

Study program: Biomedical Technology

Bachelor thesis supervisor: prof. Dr.-Ing. Jan Vrba, M.Sc.

Ivan Simeonov

Kladno 2023

BACHELOR'S THESIS ASSIGNMENT

I. PERSONAL AND STUDY DETAILS

Student's name:	**Simeonov Ivan**	Personal ID number:	**503570**
Faculty:	**Faculty of Biomedical Engineering**		
Department:	**Department of Biomedical Technology**		
Study program:	**Biomedical Technology**		

II. BACHELOR'S THESIS DETAILS

Bachelor's thesis title in English:

A Phantom Feasibility Study of Differential Microwave Temperature Monitoring of Regional Hyperthermia

Bachelor's thesis title in Czech:

Ověření proveditelnosti mikrovlnného monitorování regionální hypertermie

Guidelines:

Realize antenna elements for microwave imaging. Create a numerical model of the antenna element in contact with a homogeneous pelvic region phantom. Create a suitable experimental setup and validate the numerical model. Design several different antenna array arrangements around a pelvic phantom with a cylindrical region representing the temperature increase due to regional hyperthermia. Use synthetic data to evaluate the suitability of these arrangements in terms of temperature monitoring quality. For the most suitable configuration, create the experimental setup. Design and prepare liquid phantoms of the pelvic region and target area and measure their dielectric parameters. For different positions of the target area, measure the S-matrix of the antenna array and perform differential temperature monitoring.

Bibliography / sources:

[1] Rodrigues, D.B.; Dobšíček-Trefná, H.; Curto, S.; Winter, L.; Molitoris, J.K.; Vrba, J.; Vrba, D.; Sumser, K.; Paulides, M.M., Principles and Technologies for Electromagnetic Energy Based Therapies, ed. 1, ročník 1, kapitola Radiofrequency and microwave hyperthermia in cancer treatment, 2021, Academic Press Elsevier, ISBN: 978-0-12-820594-5
[2] Matteo Pastorino, Microwave Imaging, ed. 1st, John Wiley & Sons, Inc., 2010, ISBN 978-0-470-27800-0
[3] C. A. Balanis, Advanced Engineering Electromagnetics, ed. Solution Manual, Wiley, 1989, Chapter 2, ISBN 0471621943

Name of bachelor's thesis supervisor:

prof. Dr.-Ing. Jan Vrba, M.Sc.

Name of bachelor's thesis consultant:

Ing. Hana Laierová

Date of bachelor's thesis assignment: **14.02.2023**
Assignment valid until: **20.09.2024**

doc. Ing. Martin Rožánek, Ph.D.
Head of department

prof. MUDr. Jozef Rosina, Ph.D., MBA
Dean

DECLARATION

I hereby declare that I have completed this thesis having the topic “A Phantom Feasibility Study of Differential Microwave Temperature Monitoring of Regional Hyperthermia” independently, and that I have attached an exhaustive list of citations of the employed sources.

I do not have a compelling reason against the use of the thesis within the meaning of Section 60 of the Act No.121 / 2000 Sb., on copyright, rights related to copyright and amending some laws (the Copyright Act).

In Kladno 18.05.2023 Ivan Simeonov

ACKNOWLEDGEMENTS

I would like to thank my supervisor prof. Dr.-Ing. Jan Vrba, M.Sc. for providing me guidance and objective feedback throughout the whole process of the Bachelors thesis. His knowledge and structured ideas, combined with the great support and communication skills, provided me the best grounds to achieve the results I have. I would also like to thank Ing. Hana Laierová, M.Sc. for consulting me on how to develop the numerical simulations. Her experience on the topic provided me with the most suitable methods to evaluate the results achieved. I am also extremely thankful to Ing. Tomáš Pokorný for providing me the upmost knowledge on how to work with the reconstruction algorithm and perform the experimental evaluation.

ABSTRACT

A Phantom Feasibility Study of Differential Microwave Temperature Monitoring of Regional Hyperthermia

Microwave hyperthermia is a cancer supplementary treatment that has been researched for over two decades, as it has proven to improve the cancer treatment process significantly. This thesis aimed to study non-invasive temperature monitoring during hyperthermia in the pelvic region using Microwave Imaging technology at a frequency of 1 GHz. The feasibility of imaging the temperature changes in the heated tissue by detecting small changes in the dielectric properties, relative permittivity ε_r and equivalent conductivity σ, in the area was tested numerically and experimentally. In the software, COMSOL Multiphysics were developed multiple numerical simulations with different configurations of UWB antennas and a muscle phantom. The inverse-scattering problem was solved using a distorted Born Approximation (DBA) algorithm with a truncated singular values decomposition (TSVD). Additionally, noise was introduced to replicate the environment of the experiment. With 80 dB of noise, the numerical simulation reconstructions detected a temperature resolution of 1.55 °C, an accuracy of 97.64 % and a localisation error of 1.4 mm. Following was designed the first prototype of the experimental setup, which included a plexiglass tank with the UWB antennas attached to it, a vector network analyser (VNA) with a 24-port switching matrix and a liquid muscle phantom. The preliminary experimental reconstructions were unsuccessful, but after additional noise level measurement and matching medium (MM) testing, it was established that with proper stabilisation of the system and a different matching medium with dielectric properties $\varepsilon_r = 40$ and $\sigma = 0.7$ S/m, differential Microwave Imaging for temperature monitoring in the pelvic region with the proposed prototype is possible.

Key words

Microwave Imaging, hyperthermia, temperature monitoring

Contents

List of symbols and abbreviations **7**

1 Introduction **8**

2 Overview of the current state of the art **10**

3 Aims **14**

4 Methods **16**

4.1. Temperature dependent Cole-Cole model 16

4.2. Matching medium (MM) 17

4.3. Numerical models 18

4.4. Reconstruction algorithm and evaluation 22

4.5. Numerical model with noise 24

5 Results **33**

5.1 Configuration 1 33

5.2 Configuration 2 38

5.3 Configuration 3 42

5.4 Numerical model reconstructions with noise 46

5.5 Experiment 54

6 Discussion **62**

6.1 Numerical models 62

6.2 Numerical models with noise 65

6.3 Experiment 68

7 Conclusion **73**

References **74**

Appendix A: Contents of the attached ZIP file and the provided CD **77**

Appendix B **78**

List of symbols and abbreviations

List of symbols

Symbol	Unit	Meaning
ε_r	-	relative permittivity
σ	S · m−1	equivalent conductivity
S_{11}	-	complex reflection coefficient
S_{ij}	-	complex transmission coefficient
$\|S_{11}\|$	dB	reflection coefficient magnitude
$\|S_{ij}\|$	dB	transmission coefficient magnitude
f	GHz	frequency

List of abbreviations

Abbreviation	Meaning
MWI	microwave imaging
UWB	ultra-wide bandwidth
IPA	isopropyl alcohol
EM	electromagnetic
MR	magnetic resonance
VNA	vector network analyzer
MM	matching medium
DBA	distorted Born approximation
TSVD	truncated singular value decomposition
SNR	signal-to-noise ratio
M	measured value
R	real value
CM	convolution mask
SAR	specific absorption rate

1 Introduction

Microwave hyperthermia is currently considered to be one of the most effective means of increasing sensitivity of cancer cells to radio and chemotherapy. It has the potential to highly increase the effectiveness of the conventional treatment even with decreased dose of the primary treatment. The effect of microwave hyperthermia is proportional to the volume percentage of tumour tissue heated to 41-44 ° C for 30 to 60 minutes. Issels et al. tested the response of chemotherapy with and without hyperthermia on soft tissue sarcoma. The treatment supplemented with hyperthermia increased the response from 12,70% to 28,80% [1]. The treatment has proved a significant upside, but still has major performance challenges. On that account, it is essential that the monitoring and regulation of the temperature during the treatment is as accurate as possible. Currently, in the clinical practice, the temperature measurement during microwave hypothermia is trimmed down to invasive methods, such as thermocouples, thermistors and fiber optic sensors, and non-invasive, such as magnetic resonance (MR) [6,11]. The invasive temperature measurements are cheap and not complicated to operate with. On top of that, they provide real-time detection ability to the medical staff. Trouble with this method arises in the fact that it provides only a certain number of points in the area, while on the other hand MR thermometry provides a very accurate regional imaging of the temperature, but in addition to the high cost of MR systems, there are other disadvantages. It requires special hyperthermia applicators to be used, which would not interfere with the MRI coils [6,13].

As an alternative, microwave imaging (MWI) is a tool that is currently being researched because of the possibility of being cost effective, compact and using low power levels of non-ionizing radiation in the range of milliwatts. Because of that and the fact that the microwave technology is mature, reliable and manufactured in large volumes, the total cost of the systems is greatly reduced. One of the most important factors in an imaging system is its accessibility. The MWI has a chance to have greatly reduced size due to the incomplexity of the systems itself. It consists of the microwave measuring system VNA (vector network analyzer) and the UWB (ultra-wide bandwidth) antenna array. That proved the option to optimize the elements and improve the accessibility to a point where it could be even mobile. Finally, in medical care the most important aspect

is patient safety. MWI uses non-ionizing radiation, which has no proven harmful effects on the human body due to its low energy state.

When matter is exposed to an electric (E) field its molecules are being polarized. In the frequency range used in MWI the orientational polarization is the most dominant polarization, in which the spatial distribution of the polar molecules is changed meaning they are aligned with the E-field vector direction. The ability of any matter to interact with an electromagnetic (EM) field is expressed by the so-called dielectric properties of materials. Such properties are the relative permittivity ε_r and the equivalent conductivity σ and they dictate the way of propagation of EM waves (attenuation, reflection and phase shift) through the matter [2]. It is known that the dielectric properties of matter are dependent on frequency of the EM field and on temperature [17,18]. The MWI is a method in which the imaged area is exposed to EM waves; the reflected and transmitted signals are measured and used to reconstruct the spatial distribution of the dielectric properties or their changes in the imaged area [19]. The changes of dielectric properties due to pathologies or elevated temperature can be reconstructed using imaging algorithms, such as differential Born algorithm.

2 Overview of the current state of the art

Microwave hyperthermia has been proven over the last two decades to be the best adjuvant anti-cancer treatment. The combination with radiotherapy and chemotherapy shows a significant increase in the disease-free survival of patients in a postoperative and preoperative state [1, 4]. The raised temperature in the targeted area increases the blood perfusion rate making the cancerous tissue more susceptible to the drugs and radiation from the main treatment [1].

The microwave hyperthermia treatment effectiveness is based on the temperature that is achieved in the targeted tissue and the duration. Therefore, real-time temperature monitoring is essential for control of the accuracy and amount of power that is deposited into the body. This way it is ensured that the treatment follows the initially-given guidelines and that the patient's safety is not compromised. A study [5], conducted by Canters et al., monitored the complaints of 35 patients during regional hyperthermia treatment in the cervical area. On average 13.3 complaints about hot spots were registered per single treatment. The research also determined that SAR peaks can determine the approximate location of the hotspot complaint by the patient [5]. To control the SAR peaks, it is necessary to adjust the phase and amplitude parameters of the applicators, during the treatment. Real-time temperature monitoring will be the base of the antenna recalibrations on the fly, eliminating the potential of hot spots appearance and improperly regulated temperature in the targeted area.

When talking about temperature measurements in regional hyperthermia currently, in the clinical practice are still used both invasive and non-invasive methods. There is a big range of options in theory, but each method has its disadvantage or limitation, such as cost-effectiveness, patient comfortability and safety, or accuracy of measurement.

Invasive methods for temperature monitoring in regional hyperthermia currently, include thermocouples, thermistors, and fiber optic sensors. Thermocouple temperature sensors are based on the Seebeck effect, which states that two dissimilar metallic components in contact will produce a small voltage when a temperature change in the environment is present [6,7]. Thermocouples are cost-effective and have a fast response depending on the diameter of the probe (usually less than 1 second) [9]. In the study [8], concerning focused therapeutic ultrasound treatment, was observed that due to the high heat conductivity of the metals a significant overestimation of the temperature appears.

Another disadvantage of the method is its incompatibility with electromagnetic fields [6,7]. On top of that, metals have significantly different dielectric properties compared to soft tissues, creating an additional scattering domain for the EM waves, which challenges the reconstruction algorithm additionally. Another commonly used invasive method for temperature monitoring is using the thermistors. Thermistors are semiconductors that experience a non-linear change of resistance with the temperature change. They provide better response time and accuracy than thermocouples and are inexpensive. On the other hand, the size of the probe is larger and the relation, as already mentioned, is non-linear [10]. Finally, the third method of invasive thermometry during hyperthermia treatment is using fiber optic sensors (FOSs). The FOSs have a significant advantage over the previously mentioned electrical sensors in the fact that they are produced from Silica Glass, therefore no thermal conduction error will be present. Also, the glass or polymer material makes the probe electrically immune to the electromagnetic field, making it compatible with hyperthermia systems [9]. The FOSs are current gold standard in invasive temperature monitoring although they are still under major development and implementation. Issues like the small spatial resolution (about 0.5 probes per centimeter), cross-sensitivity to strain caused by breathing, and high price, are still limiting the wide spread of the method [6,9]. The main disadvantages of the previously mentioned methods are their invasiveness, which causes uncomfortably for the patient and additional work for the clinician, and the low spatial resolution because the methods allow only single-point measurements.

Non-invasive methods for temperature monitoring in regional hyperthermia used in the current clinical practice include only magnetic resonance (MR) thermometry. There are many methods for the computation of the temperature using different parameters of the MR. The most common method is using the proton resonance frequency (PRF) of water molecules [12]. Change in MR phase has an oppositely proportional dependence to the temperature change in the following way: 4.70° phase difference between two points per ° Celsius, as established in [11]. The advantage of the non-invasive methods is that it creates a 3-dimensional temperature monitoring map, which is a great tool to have in regional hyperthermia treatments. The problem that arises with MR thermometry is the cost-effectiveness and compatibility of the microwave hyperthermia system with the superconductive electromagnet of the MR. As shown in [14], regular applicators cause major distortions in the temperature monitoring results. Therefore, to integrate MR

thermometry, the hyperthermia system needs to adapt applicators such as the one proposed here [15] and have special MR-compatible spatial dimensions. This leads to the current state of the art - MR-hyperthermia system, which is the currently most advanced mean of temperature monitoring during microwave hyperthermia in the world [16]. The incompatibility and operation price, as previously mentioned are still the main limitations of the system to be widely used in clinical practice.

An alternative for non-invasive thermometry during HT is differential microwave imaging (DMWI). DMWI system uses non-ionizing radiation, is cost-effective, due to the massive worldwide production of radiofrequency components, and has a chance for relatively small dimensions because of its incomplexity. In terms of using the systems as a means of thermometry is proven possible by the fact the dielectric properties of matter are temperature dependent, especially in a broad frequency band [17,18]. Numerous studies, like [17] for biological tissues, illustrate a replicable relationship in the operating range of MWI between 0.5 GHz to 7 GHz and in the temperature range that is applicable, from 30 °C and 50 °C. In the early stages, the upside of the method is demonstrated in a study [19] with a pig and a tube of saline solution running through the abdomen section, where only the equivalent conductivity was monitored. Sixteen monopole antenna array was put around the body and frequencies from 300 MHz to 1 GHz were used and the system provided a resolution of 1 °C at 900 MHz. It was concluded that the results are extremely dependent on the imaged area complexity of dielectric properties, but a real-time microwave imaging system has promising potential. Later in [20], a real-time 3-D differential MWI thermometry system was designed with 36 antennas around an enclosure with a radius of 15 cm. The imaging frequency was 915 MHz, while a temperature change of 25 °C was introduced. The system had a resolution of 1°C and a 4-second refresh rate, therefore considered close to real-time for the purpose of therapeutic heating. Additionally, in [21] was proposed a new ultra-wide bandwidth (UWB) bowtie antenna that is currently accepted as gold standard for MWI (See Fig. 2.2). It is designed specifically for the frequency range of 1-6 GHz and has a balanced-to-unbalanced circuit, or the so-called balun, that compensates for the unsymmetrical feeding of the coaxial cable. The reflection coefficient |S11| is lower than -12 dB for the whole range, therefore the antenna possesses great radiation efficiency [3, 21].

The state of the art of MWI thermometry is yet to reach its peak and although there are a few feasibility studies, like the ones mentioned above, there are still many open

issues. Such are that bigger imaged areas have not been tested (e.g., pelvic region) and also small dielectric properties changes such as from regional heating of 8 °C, have not been imaged as of yet. These problematics will be addressed in this paper.

3 Aims

The main goal of this bachelor's thesis is creating computational and experimental setup to test the numerical and consequentially experimental feasibility of differential microwave imaging (MWI) technology for non-invasive real-time temperature monitoring in the pelvic region during hyperthermia treatment. The aim is to provide evidence that such a system is able to detect slight changes in the dielectric properties of tissues due to the increase in temperature with reasonable accuracy, qualitatively and quantitatively.

First, 3-D numerical models will be created, with different antenna arrangements and suitable matching medium (MM) that will allow the microwave power to be transferred appropriately into the phantom with adequate transmission coefficients $|S_{ij}|$ between the antennas. How well that is done will be evaluated through the achieved scattering matrix. After that, the reconstruction algorithm, distorted Born approximation (DBA), must be applied to solve the inverse scattering problem and reconstruction of the first images will be done. Additionally, simulated noise for different levels will be introduced to approximate the experimental environment. Finally, the numerical reconstructions are to be analyzed qualitatively and quantitatively; providing the proper localisation and size of the heated area and detecting an 8 °C temperature change with a resolution lower than 1.5 °C. These results will be used to prove the method's feasibility and provide ground for the experimental study.

After that, the experimental setup preparation will begin. That includes assembling the set of UWB bowtie antennas from the fabricated components. After being prepared, they should be tested for suitability with the MWI system, meaning reflection coefficients |S11| should be lower than -10 dB at all imaging frequencies: 0.8-6 GHz. Next, the reflection coefficients of each antenna component are tested in distilled water. The antennas that cover the requirements will be used in the experimental setup. Following that will be designed and 3-D printed holders for the antennas that will attach to the plexiglass tank, where the liquid phantom will be placed. The holders will be subsequentially glued to the plexiglass tank.

Two liquid phantoms will be created representing the dielectric properties of heated muscle tissue at 45 °C and analogically of the non-heated external tissues at 37 °C. The

properties must be as close as possible to the values predicted with a single-pole Cole-Cole model of the muscle tissues used in the numerical simulations to create a similar environment. Distilled water, isopropanol (IPA), and salt will be used to realise the phantoms. The exact values have to be obtained by testing. The liquid simulating the target (heated) area will be placed in a plastic cylinder that will be inserted in the tank with the exact position. Using a 24-channel vector network analyser (VNA), the S-matrix will be measured in two stages. Firstly, a homogenous medium with dielectric properties of a muscle at 37 °C will be measured. Following that, the cylinder representing the heated area will be inserted, and another measurement will be performed. The first experimental reconstruction will be created with the E-fields extracted from the simulation and the two recorded scattering matrices. The same parameters as in the numerical reconstructions will be evaluated. The comparison between the numerical and experimental values will be discussed and conclusions about the feasibility will be made.

4 Methods

4.1. Temperature dependent Cole-Cole model

Dielectric properties of tissues exhibit both frequency and temperature dependency [17]. In [17], the dielectric properties of animal tissues (animal liver, muscle, fat and blood) in the microwave frequency range from 0.5 GHz to 7 GHz and in the temperature range from 30 °C to 50 °C were measured. Furthermore, an extension of the Cole-Cole model with temperature dependency was proposed, and the measured values were approximated by this modified model. The difference between a single-pole Cole-Cole and a two-pole Cole-Cole in this range is small and the temperature dependence of the muscle tissues in the considered temperature range is nearly linear. Because of that, the method proposed in [27] was utilized to establish a golden standard for simulating the heated tissue and evaluating the results of the microwave image reconstruction. (See Figure 4.1).

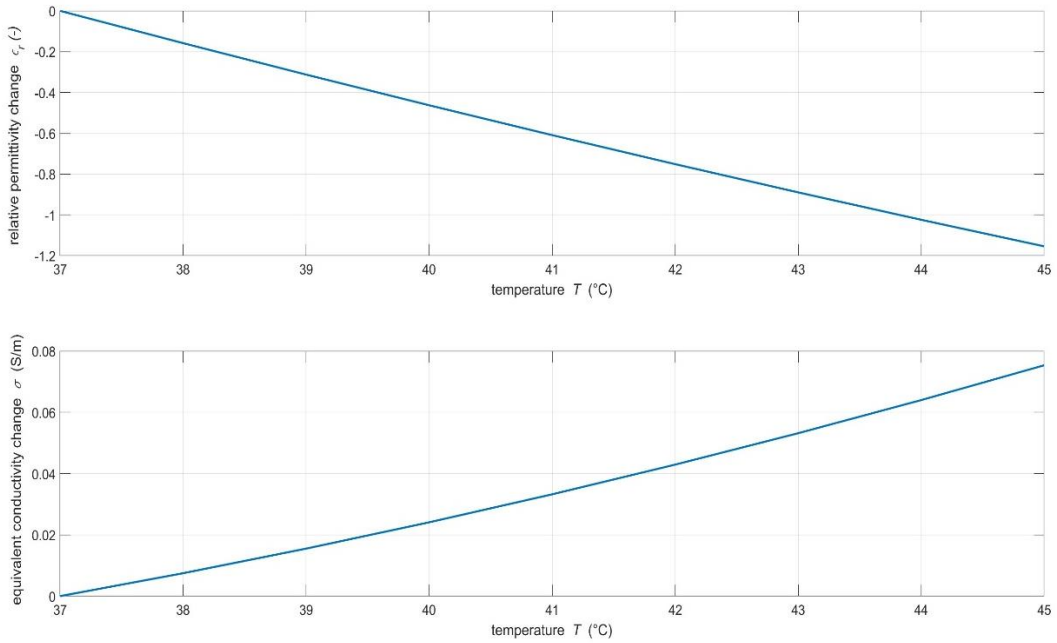

Figure 4.1: Single-pole Cole-Cole model, approximating the temperature dependence of the relative permittivity ε_r (-) and the equivalent conductivity σ (S/m) of muscle tissue [17,27].

4.2. Matching medium (MM)

In microwave-based imaging techniques it is essential to use a proper matching medium between the antenna and the tissue in order to establish a proper transfer of the EM power. Therefore, creating a good matching medium will have a direct effect on the image quality. In the study [28] the reflection coefficient $|S_{11}|$ with a significant mismatching medium and a matching medium creating a smooth transition was compared. Even though, the experiment was done on adipose tissue, which has relative permittivity $\varepsilon_r = 5$ (-), relatively significant change in the reflected power was observed. Muscle has a relative permittivity of 54.8 (-), significantly higher than adipose tissue, thereby making the transfer of EM power harder and more important [22].

Currently, there is no information on the best matching medium for microwave-based imaging in the pelvic region, therefore multiple matching liquids were tested in the numerical studies with a goal to determine the most suitable one for this purpose. As a guidance for the testing was used [29], where was created a multiplanar model of human tissue and the reflection $|S_{11}|$ and transmission $|S_{ij}|$ coefficients were measured with different matching mediums. It was determined that a lossless matching medium would be hard to accomplish, although values of relative permittivity ε_r between 5-30 (-) and equivalent conductivity σ (S/m) lower than 0.2 S/m are suggested [29]. It must be considered that in the following numerical models was determined a suitable MM, where between the tissues and UWB antennas is present a plexiglass cage. The MM was specifically designed to provide the proper propagation of EM power through the plexiglass, therefore can be applied only for this feasibility work.

4.3. Numerical models

In order to calculate electromagnetic fields in the imaged area and corresponding S-parameters needed for the imaging, a numerical model was implemented in the simulation software COMSOL Multiphysics [27]. It consists of a plexiglass cage, irregular octagon shape, where the phantom is placed and 12, 24 or 22 UWB antennas, developed in [21], in multiple configurations that will be shown later. Inside the plexiglass is placed a muscle phantom with dielectric properties described by the one-pole Cole-Cole [17, 27] at 37 °C and a cylinder (radius of 5 cm), representing the heated area, of muscle tissue at 45 °C with analogical dielectric properties (see Figure 4.1). All of the models below operate on 1GHz frequency, as it was determined to be the best-working resonant frequency for the UWB antennas [21].

The geometry of the model was changed in terms of the UWB antenna placement and distribution. The antenna holder cage [27] was removed and they were moved directly on the plexiglass's tank outer surface with a matching medium in-between as seen in Figure 4.2. The purpose of that is to improve the SNR and to increase the EM power transfer into the phantom. In [27], the antenna elements are directly in contact with a water bolus surrounding the whole pelvic phantom. The coupling of antennas through the water bolus was thus significant (consultation with Prof. Jan Vrba and Ing. Hana Mozerova), leading to worse image reconstruction results. As shown in [31], antennas that are located in a single compartment, exhibit a mutually coupling behaviour, distorting the results. The solution proposed there is to place the antennas in a different configuration, but it was decided to create an individual compartment with matching liquid for each of the UWB antennas (consultation with doc. Dr.-Ing. Jan Vrba, M.Sc and Ing. Hana Mozerova). The compartment covers the whole front face of the antenna and is 2 cm thick. For the numerical simulations it was not necessary to create a holder, that will keep the components and the matching medium in place, but for the experimental setup it was developed, which will be presented later in the paper.

As a starting point, the first tested geometry, included 12 UWB antennas [21], placed on a single plane.

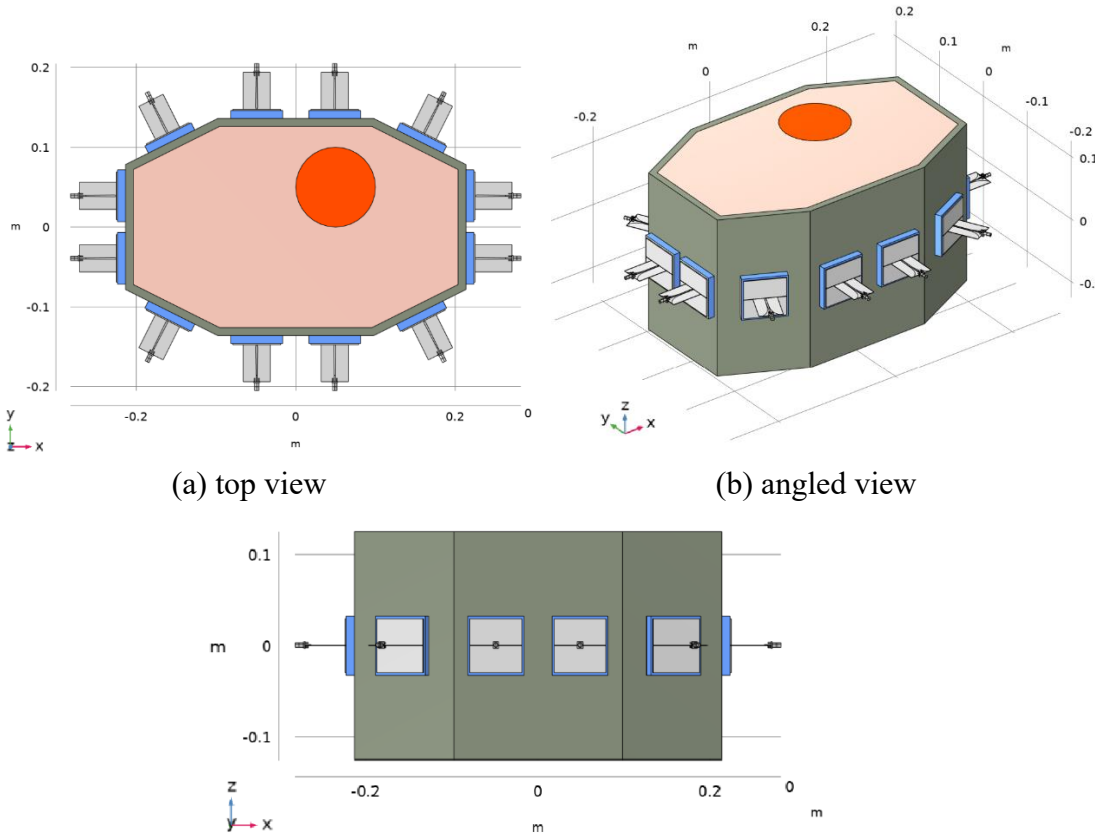

(a) top view

(b) angled view

(c) side view

Figure 4.2: Geometry of a MWI model in COMSOL Multiphysics with 12 UWB antennas in a single plane, operating at a frequency of 1GHz, where: heated muscle phantom (45 °C) - orange, non-heated muscle phantom (37 °C) – pink, plexiglass cage – grey, MM – blue. Referred to as Configuration 1.

Following the first geometry, a similar geometry consisting of 24 UWB antennas placed in two rows above each other, with the purpose of gaining more volumetric information of the phantom (see Figure 4.3). It was, also proposed to interpolate the 2 rows of antennas by shifting sideways one of them (consultation with doc. Dr.-Ing. Jan Vrba), however that was not implemented, as the size of the elements was limiting significantly the number that could be placed. Unfortunately, later was found out the reconstruction algorithm and imaging would limit the possibility of showing the volumetric results completely which will be discussed further later.

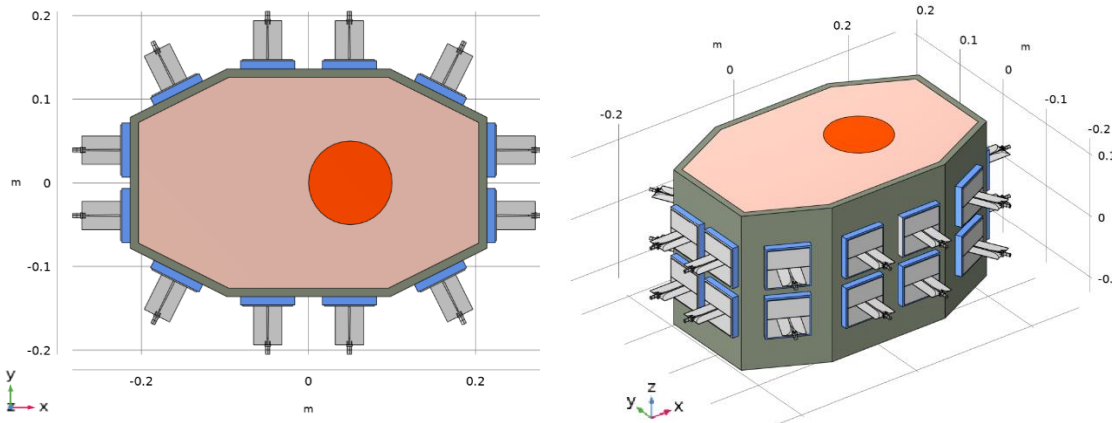

(a) top view (b) angled view

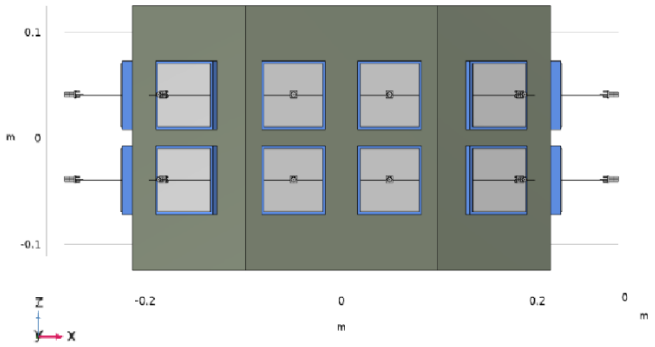

(c) side view

Figure 4.3: Geometry of a MWI model in COMSOL Multiphysics with 24 UWB antennas (12 on each plane) operating at a frequency of 1GHz, where: heated muscle phantom (45 °C) - orange, non-heated muscle phantom (37 °C) – pink, plexiglass cage – grey, MM – blue. Referred to as Configuration 2.

Due to the limitation mentioned above was proposed to continue with single plane imaging for now. Assoc. Prof. Ondrej Fiser [21], proposed to reduce the size of the antennas horizontally, as that should have no effect on the bowtie antenna performance and it will allow for more antennas to be placed on the system horizontally. Therefore, the final geometry utilizes a new reduced size antenna element.

The geometry consists of 22 UWB antennas placed in one plane similarly to Figure 4.2, with the purpose of increasing the imaging quality and resolution to a maximum on a single plane (see Figure 4.4). That was the last geometry that was tested in this study.

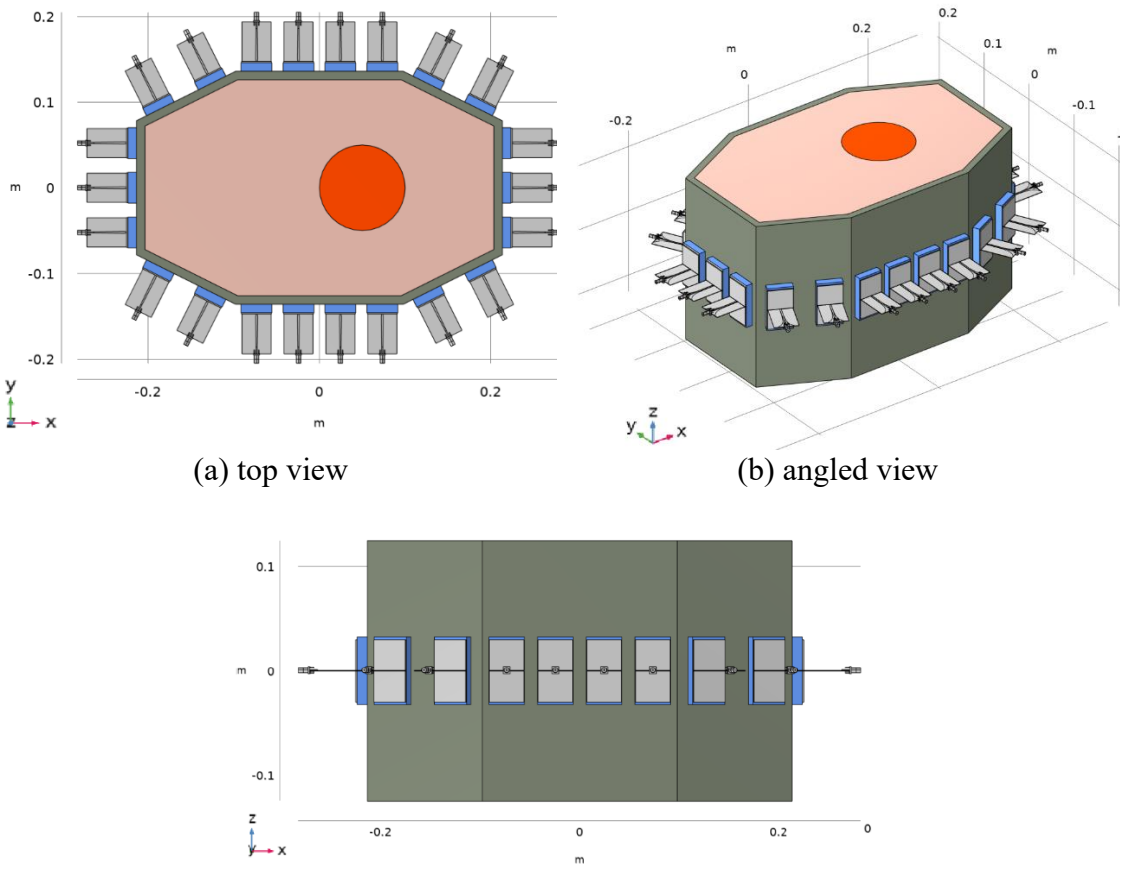

(a) top view (b) angled view

(c) side view

Figure 4.4: Geometry of a MWI model in COMSOL Multiphysics with 22 UWB antennas in a single plane, operating at a frequency of 1GHz, where: heated muscle phantom (45 °C) - orange, non-heated muscle phantom (37 °C) – pink, plexiglass cage – grey, MM – blue. Referred to as Configuration 3.

4.4. Reconstruction algorithm and evaluation

Solving the inverse scattering problem for large areas of biological tissues was proven to be hard, due to the following reasons. The scattered fields can be measured only in a small area outside the object domain. When simulating the propagation of electromagnetic waves the diffraction effects of microwaves must be taken into account. It is impossible to reduce the wave to a ray because of the large wavelength, which is few times smaller than the object. The strong contrast between the external layers and the surroundings also makes it easy to conceal the contribution of the inner body components [30].

For image reconstruction an algorithm based on distorted Born approximation (DBA) with truncated singular value decomposition (TSVD) was used, as proposed in [27, 32]. This imaging algorithm is precise enough and does not require long computational time, therefore it is suitable for our purpose.

Differential Microwave imaging system for temperature monitoring in hyperthermia treatment must provide accurate information about the size, location and exact temperature of the heated area. Therefore, as far as image evaluation goes, the results were be evaluated in terms of quantity and quality. The two parameters, namely relative permittivity ε_r and equivalent conductivity σ, were evaluated separately with the purpose of identifying trends and effects of the different matching mediums on each of them.

Quantitative evaluation was performed by comparing the actual differential values ($\Delta\varepsilon_r$, $\Delta\sigma$) derived from the single-pole Cole-Cole model (see Figure 4.1) and the results from the reconstruction. All the pixels in the region of heating are averaged out and the Percentage error is calculated:

$$\delta = 100\frac{(M - R)}{R} \tag{4.1}$$

The same process is done for the area outside the region of interest to measure the artefacts and noise, although due to the characteristic of the Percentage error formula, a number cannot be compared to zero. Therefore, just the average value of both parameters is calculated.

Qualitative evaluation is not, as straight forward, as it implements thresholding image processing, as done in [27], in order to segment the target area. The standard value

proposed in [27] is -3 dB, but also a lower threshold can be tested at -6 dB. Another processing tool that was used before the evaluation to remove artefacts which exceed the threshold range, therefore were identified, as a heated area, is the morphological opening which clears small groups of pixels that could not be part of the heated area. The qualitative evaluation will produce multiple parameters including sensitivity, specificity and accuracy. These parameters are useful, as long as, we have information about the proper localization. In that case, are evaluated two more parameters: area ratio (-) and localization error (mm). Area ratio describes the area that is classified as target with respect to the area of actual target, while the localization error represents the distance between the centre of gravity of the retrieved contrast and the actual centre of gravity of the heated area [27], meaning that, the quantitative retrieved contrast is used while only pixels of the target are taken into consideration.

4.5. Numerical model with noise

The main aim of creating the numerical models was to simulate, as closely as possible to experimental setup. Although the geometry of the models is identical to the experimental hardware, simulation software, like COMSOL Multiphysics assumes perfect environment conditions and implements a finite element analysis. In reality the environment introduces noise disturbances and the measurement results are not approximate to then simulation solutions. To counteract that, the best performing simulation model from Chapter 4.3 and the reconstruction algorithm were modified additionally.

Firstly, the heated muscle liquid phantom must be placed in some kind of a casing, which would prevent it from spilling and meshing with the non-heated phantom. Therefore, for that was decided that a plastics polyvinyl chloride (PVC) tube with 10 cm radius and 4 mm thickness of the walls will be introduced into the models. Since no information was found on the dielectric properties of PVC at 1GHz, it was assumed that it is in close proximity to plastic: $\varepsilon_r = 2.6$ and $\sigma = 0.01$ S/m. The scattering gradient created by the material is significant, therefore even though the dielectric constant is not exact it still provided functional information. The tube was introduced to both the homogenous and non-homogenous (with heated area) models because of the fact that the reconstruction method is differential, meaning that everything that does not change with time must remain, as similar as possible so that the algorithm does not recognise it, as an unwanted change.

Additionally, through MATLAB, after extraction of the E-fields and S-matrices from COMSOL Multiphysics was added noise, before performing the reconstructions. That was done with the function *awgn()*, which allows to introduce white Gaussian noise with any power desired into the data. Multiple noise levels were used with the goal to find out the maximum noise level that can be introduced, which will still allow the Born approximation algorithm to create a reasonably accurate reconstruction. Multiple matching mediums were tested to see how changing their properties can also affect the noise reduction. The noise powers tested were from 110 dB to 80 dB with a step of 10 dB. The evaluation of the results is performed in the same way, as mentioned in Chapter 4.5, and comparison between the models without noise and with added noise was made, to evaluate its effect.

4.6. Experiment

In this chapter is the preparation of the experimental setup for the Microwave Differential Temperature monitoring system. Here is be described the development of the hardware including materials used and complications in the process. The system is identical to the models created, which includes a plexiglass tank, 22 UWB antennas [21], muscle liquid phantom and a 24-port VNA with a switching matrix. This first section includes the assembly of the UWB antennas that were be used in the system

4.6.1. Assembly and testing of the UWB antennas

The UWB antennas designed in the study [21] were used. The assembly was performed with the following tools: epoxy glue and WEP 852D 700W Soldering Station. The bowtie arms were carefully soldered to the balun circuit which had already been soldered to the coaxial connector in the fabrication of components process. After that using the epoxy glue, 4 yellow 3D printed supports were glued under a slight angle (2 on each side of the balun circuit) between the plane that holds the bowtie arms and the plane that has the balun circuit attached to it (See Figure 4.5).

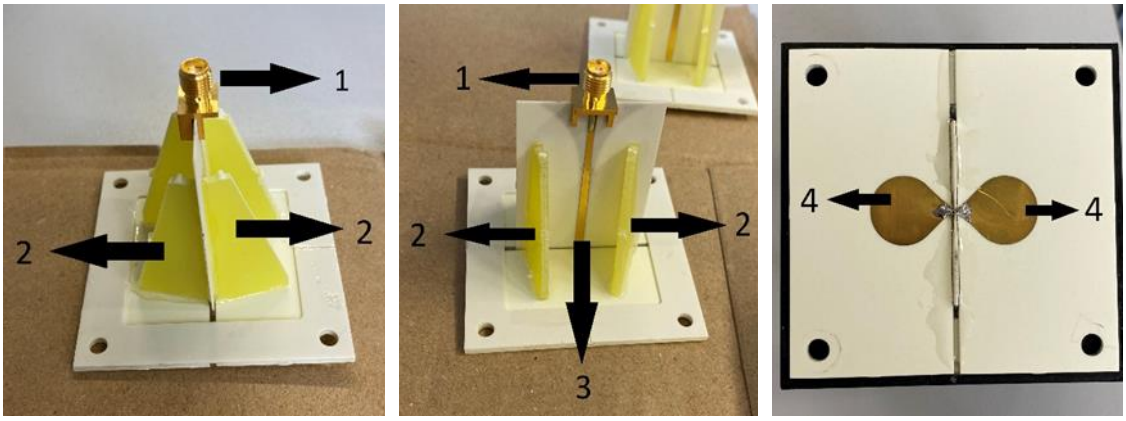

(a) (b) (c)

Figure 4.5: Photos of the assembled UWB bowtie antenna (a) side view, (b) front view, (c) top view, where: 1 – coaxial connector, 2 – side supports, 3 – balun, 4 – bowties arms.

Due to the development of the models, as mentioned in Chapter 4.3, the size of the antennas was reduced by 1cm on each side. That allowed to place more of the in a single plane around the phantom but would not influence the performance. Following that each antenna had its reflection coefficient $|S_{11}|$ (dB) measured. The antennas would be tested in direct contact with liquid; therefore, a thin layer of epoxy glue was placed on the soldering of the bowtie arms to prevent rusting. Each antenna was numbered given enough time, so the glue had fully dried and the testing could take place.

The reflection coefficients $|S_{11}|$ (dB) of the UWB bowtie antennas were measured in contact with distilled water. To perform the measurements was used the following two channel vector network analyzer (VNA) modality: Rohde & Schwarz VNA FSH8, coaxial cable, stand with a holder, and a deep box. A frequency band from 0.8 GHz to 6 GHz with 10 kHz step had been set up for the measurement. The coaxial cable was attached in a stable way to limit movements causing artefacts. The calibration kit Rohde & Schwarz ZV-Z135 Female was used for the recalibration after each 4 measurements, because during the exchange of the antenna elements to be measured, it was not possible to prevent small movements with the measuring coaxial cable. The setup for the testing can be seen in Figure 4.6. The antennas were in direct contact with the liquid not more than 2 mm deep from the liquid upper surface (See Figure 4.7). It was ensured that there were no air bubbles between the antenna surface and the liquid as they can create an additional scattering surface.

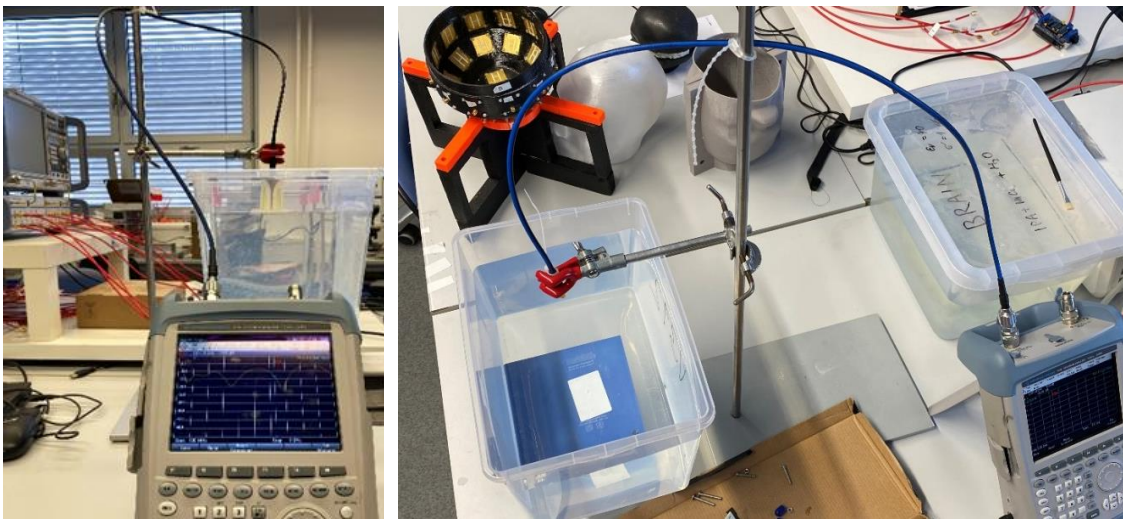

Figure 4.6: Experimental setup for measuring the reflection coefficients $|S_{11}|$ (dB) of the UWB bowtie antennas in contact with distilled water.

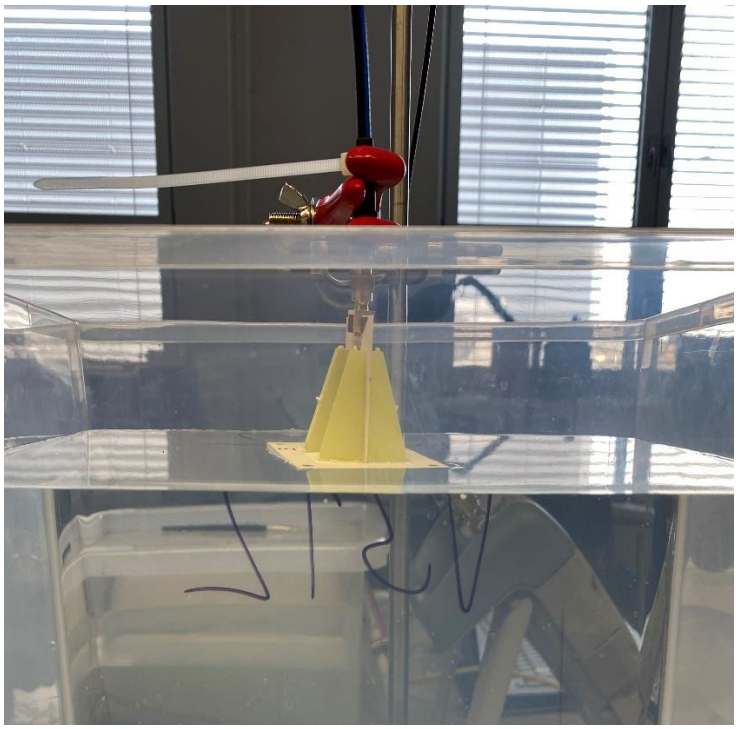

Figure 4.7: UWB bowtie antenna in contact with distilled water during reflection coefficient $|S_{11}|$ (dB) measurement.

The data was exported from the VNA in a SET file format. Since MATLAB cannot operate with this format the measurements were converted to S1P. The plotting and analyzation of the $|S_{11}|$ parameter was performed in MATLAB using the RF toolbox. Two graphs were computed: average reflection coefficient and individual reflection coefficients. The goal was to monitor whether all the antennas exhibited similar behavior and had a reflection coefficient $|S_{11}| < -10$ dB, which corresponds less than 10% of the power being reflected back, meaning they were suitable for the system.

For the experimental testing of the system an antenna holder was designed and 3D printed, which would hold the matching liquid and the antenna in place. The holder design was developed in the platform COMSOL Multiphysics with respect to the reduced size UWB antenna elements. The design was made in such a way that the horizontal space it occupies was as small as possible to be able to fit, as many antenna elements horizontally, as possible. The opening on the top allows for the matching liquid to be conveniently poured and removed. Plastic screws with applied epoxy glue, to prevent leakage, fix the antenna tightly to the holder (see Figure 4.8).

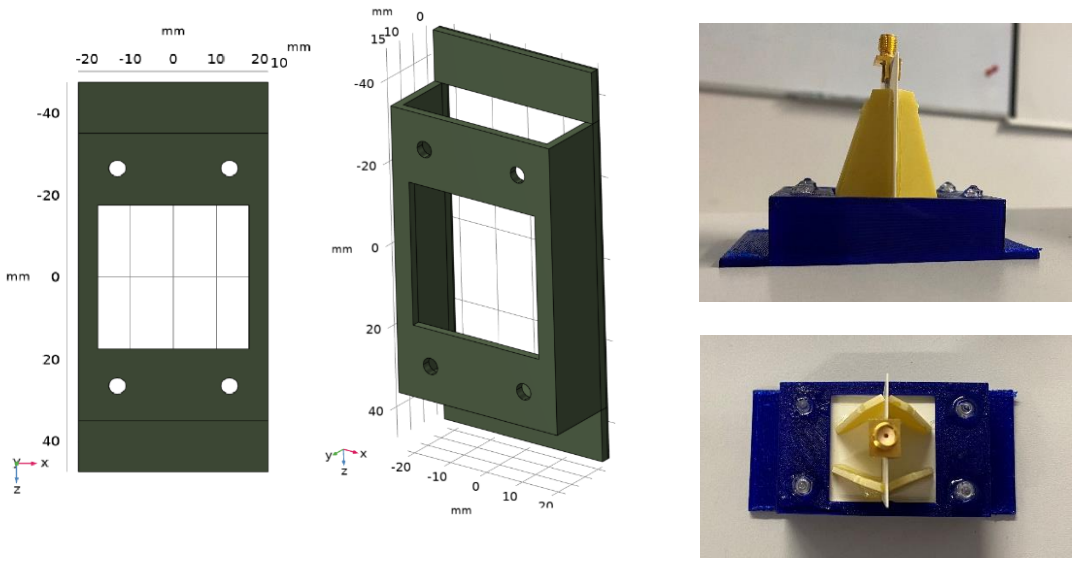

(a) (b)

Figure 4.8: UWB antennas holder design in COMSOL (a) and 3-D printed fitted and glued onto an UWB antenna (b).

4.6.2. Muscle liquid phantom

The preparation of the liquid muscle phantom was based on a similar principle to the one in [23], where isopropyl alcohol (IPA), distilled water and salt (NaCl) were used. The desired values for the dielectric properties were derived from the single-pole Cole-Cole described in Chapter 4.1 (See Figure 4.1). Since the dielectric properties experience extremely small changes in the temperature range from 37 °C to 45 °C, establishing the exact dielectric properties in large volumes of liquid was a demanding and complex task. The goal was to achieve values, as close as possible to the ones used in the model but also to establish a buffer, which would allow to still obtain some kind of contrast despite the standard deviation.

The relative permittivity of the IPA is $\varepsilon_r = 20$, therefore it was used to initially decrease the permittivity of the distilled water [24]. After that NaCl is used to increase the conductivity of the solution to the desired value stated above. Ten measurements were performed with one minute interval between them to let the solution become stable. For the measurement was used the Dielectric Assessment Kit (DAK 4 MHz – 3 GHz) from SPEAG [25]. Mixing IPA and water created an exothermic reaction and the solution heated up to 38 °C, leading to evaporation of some of the IPA and increase in the relative

permittivity. Because of that the solutions were prepared prior to the day of the measurement and were measured and adjusted right before the measurement. The solution was also constantly stirred since the IPA is less dense than water, so it flows to the top, while the salt sits at the bottom. The exact ratio of the components of the solution can be found in Table 4.1. The volume of the tank is 27 L, so 10 L of IPA, 20 L of distilled water and 120 g of salt were used. The liquids were kept in a cool room in tightly sealed 5 L bottles to prevent any evaporation of the IPA.

Table 4.1: Ratios of the components used to create two muscle liquid phantoms representing a temperature of 37 °C and 45 °C at frequency of 1 GHz.

phantom (°C)	relative permittivity ε_r (-)	equivalent conductivity σ (S/m)	IPA (%)	salt (g/L)	distilled water (%)
37.00	54.21	0.72	30.25	3.82	69.75
45.00	53.06	0.80	35.20	6.01	64.80

The shown dielectric properties are target values, not the actual achieved values. Actual values can be found in the section Results. IPA: isopropyl alcohol.

4.6.3. Realization

The realization of the experimental setup began by choosing the appropriate components to create the container which will introduce the muscle phantom with an increased temperature into the homogenous 37 °C phantom. The container had to be waterproof and have a way of being exactly positioned. A PVC pipe with a diameter of 10 cm and 4 mm thickness of the walls was chosen (see Figure 4.9 (a)). To enclose it on the bottom in COMSOL was designed the geometry seen in (c) and 3-D printed. It has 5 pins that will hold the pipe straight and position it on the positioning plexiglass board (see Figure 4.10). The cap has thick bottom and sides to be able to withstand the high pressure created by the liquid in the plexiglass tank. To seal it additionally was used MAMUT GLUE Crystal, which is a silicone-based glue.

(a) pipe (b) top cap (c) bottom cap with positioning pins

Figure 4.9: Components used for the container holding the increased temperature phantom [33].

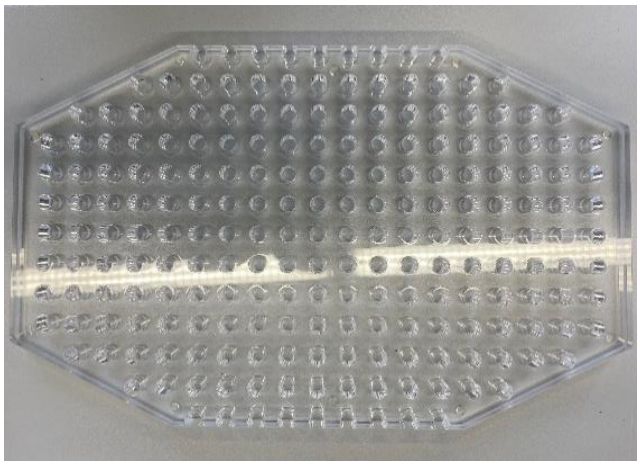

Figure 4.10: Board for container positioning.

The previously mentioned glue was additionally used to waterproof the back side of the antenna components (see Figure 4.11). After drying the placement on the plexiglass tank began. An outline was created for the exact positions with a marker. The MAMUT GLUE Crystal was used to fix them. Following that liquid was introduced into each MM compartment to ensure there is not leaks. The complete experimental setup can be observed in Figure 4.12.

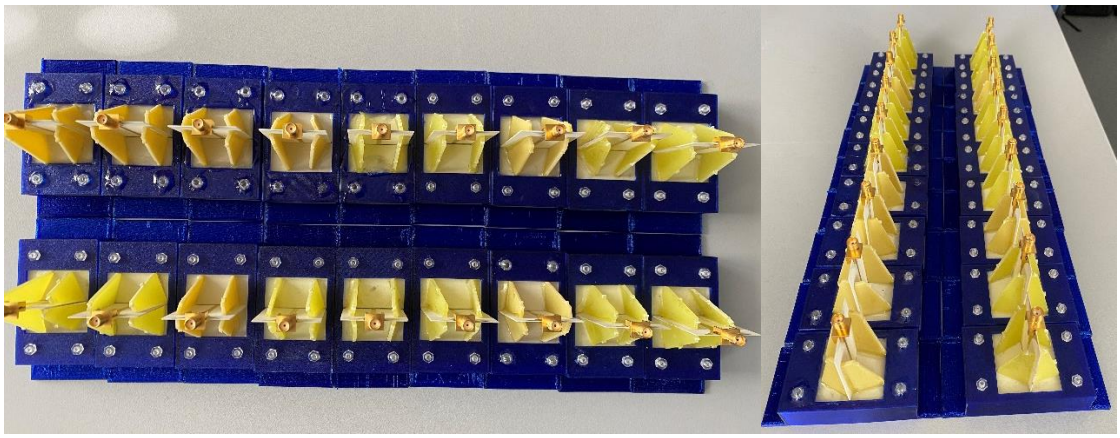

Figure 4.11: UWB antenna components with a 3-D printed holder attached.

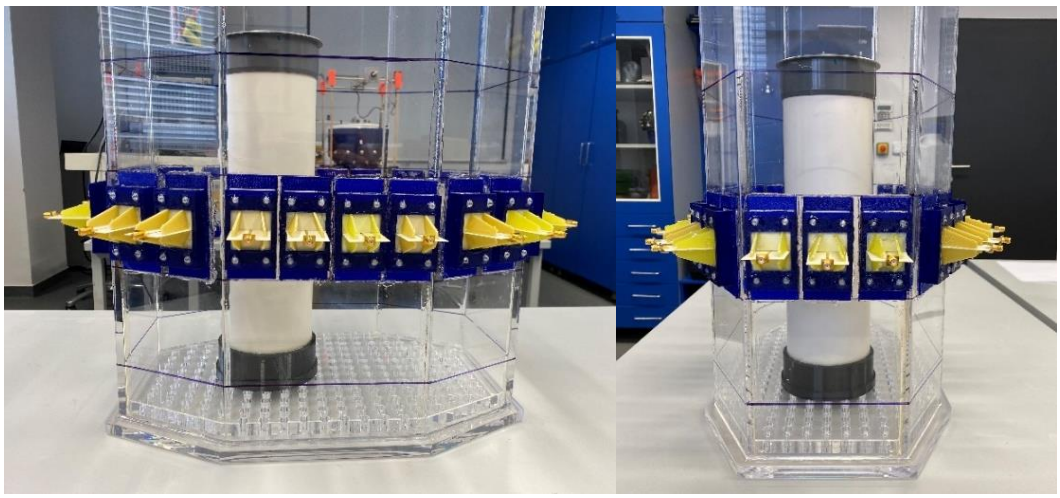

Figure 4.12: Complete preliminary prototype of the experimental setup.

For the measurement was used the Rohde & Schwarz ZNB-8 Vector Network Analyzer [34] with a 24-channel switching matrix. The 22 coaxial cables were initially connected to the antennas in the best fitting way. After that the calibration was performed using a calibration unit with 5 ports and 1 common port. As it has only 5 ports, a schema for the calibration was created, which was inputted in the VNA before beginning the calibration, so the device can recognize which channels were being calibrated. Using a peristaltic pump all the liquids including the matching medium were introduced into the tank and analogically the holders (see Figure 4.13).

Figure 4.13: Operating experimental setup.

After continuous stirring the first measurement was taken, which is only of the homogenous tank filled with the 37 °C muscle phantom. The data was directly saved in a MATLAB matrix. In the next measurement was introduced the heated area. The liquid was first poured into the container and then manually inserted into the positioning board. That proved to be a complex task since the plastic of the container was floating up, so it had to be attached tightly into the holes with a bit of force. The second measurement with the introduced non-homogeneity was also performed. During both measurements was used a 100 Hz IF bandpass filter integrated in the VNA.

The first reconstruction was done using the distorted Born Approximation algorithm described in Chapter 4.4. The inputs of the algorithm are the S-matrix from the measurement without heated area and the S-matrix from the measurement with the heated area introduced. Additionally, for reconstruction the DBA requires the electric fields in the whole imaged area, which we had no means available to measure, therefore the electric fields were exported from the equivalent numerical simulation model. After, the reconstructions and the differential S-matrix were compared to the numerical reconstructions with introduced noise level to draw conclusion for the feasibility of the Differential Microwave Imaging method for temperature monitoring in the pelvic region.

5 Results

5.1 Configuration 1

For the first geometry was tested a bigger range of MM properties in order to get an overall idea of effect to the qualitative evaluation. It was expected that the quantitative results would not have given much information at this stage, as the imaged area is big, while the antenna sources are just 12. Because of that for qualitative evaluation was used a thresholding of -3dB to filter out the expected big artefacts in the non-heated region (Table 5.1). The most appropriate TSVD was chosen as 45, where the maximum is calculated depending on the number of antennas [27]:

$$TSVD_{max} = \frac{N * (N - 1)}{2} \tag{5.1}$$

Also, a convolution mask (CM) of 3x3 of ones with the function *ones()* in MATLAB was implemented into the reconstruction algorithm. As for this study the two parameters relative permittivity change $\Delta\varepsilon_r$ (-) and equivalent conductivity change $\Delta\sigma$ (S/m), were separately evaluated and imaged. The image reconstruction only for the best MM for each situation is shown (see Figure 5.2). Due to the low variability the value specificity was excluded from the measurement results, as it does not provide any qualitative information in all models.

5.1.1 Relative permittivity evaluation of Configuration 1

Table 5.1: Qualitative evaluation of the total permittivity change $\Delta\varepsilon_r$ (-) for 12 UWB MWI differential temperature monitoring model using a threshold of -3 dB, with the following image reconstruction parameters: TSVD = 45, CM = *ones(3)*; and different matching mediums.

MM properties		sensitivity (%)	accuracy (%)	area ratio (-)	localization error (mm)
ε_r (-)	σ (S/m)				
20.00	0.30	60.52	96.65	0.61	1.00
50.00	0.10	55.66	96.24	0.56	4.97
35.00	0.50	77.35	98.08	0.77	0.90

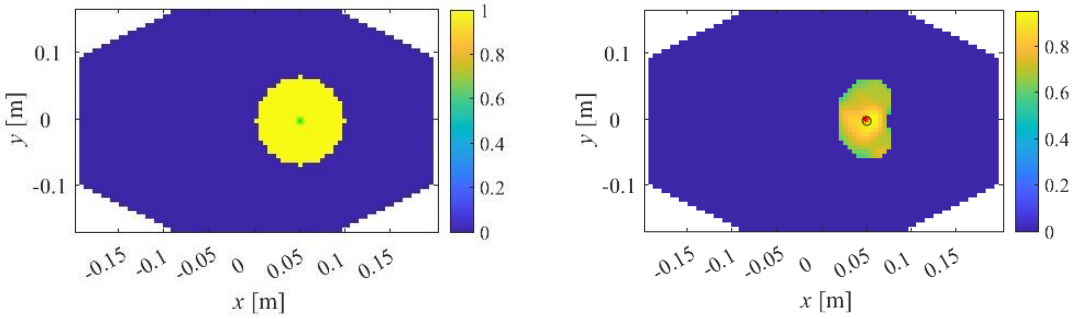

(a) actual binary mask (b) retrieved binary mask + contrast

Figure 5.1: Results of qualitative image evaluation of total permittivity change $\Delta\varepsilon_r$ (-) in Configuration 1 with MM of ε_r = 20 (-) and σ = 0.3 (S/m), with -3 dB threshold, where the green pixel is actual center of gravity, while the red one is retrieved center of gravity.

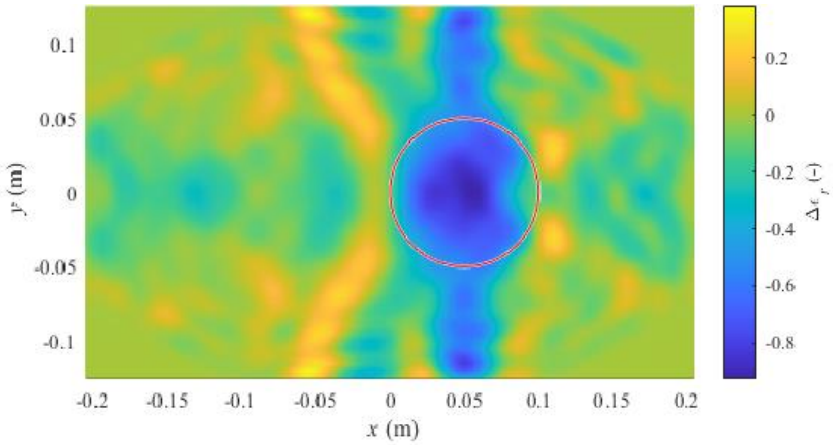

(a) 2-D

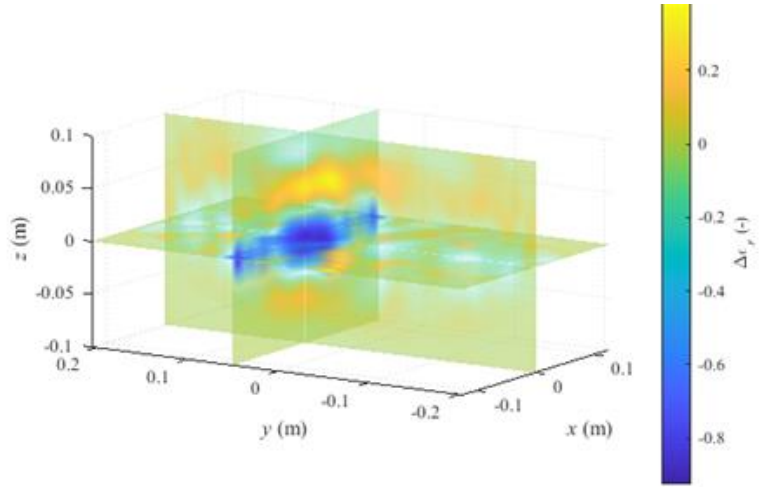

(b) 3-D

Figure 5.2: Image reconstruction of total permittivity change $\Delta\ \varepsilon_r$ (-), for MM with parameters ε_r = 20 (-) and σ = 0.3 (S/m). The TSVD is 45 and the CM is *ones(3)*.

Table 5.2: Quantitative evaluation of the total permittivity change $\Delta\varepsilon_r$ (-) of Configuration 1 for different MM parameters. The TSVD is 45 and the CM is *ones(3)*.

MM properties		$\Delta\ \varepsilon_r$ in the	quantitative	$\Delta\ \varepsilon_r$ outside the
ε_r (-)	σ (S/m)	heated area (-)	error $\lvert\delta\rvert$ (%)	heated area (-)
35.00	0.50	-0.53	54.10	-0.06
50.00	0.19	-0.63	45.14	-0.06
20.00	0.30	-0.62	46.33	-0.07

5.1.2 Equivalent conductivity evaluation of Configuration 1

Following is the image evaluation of the equivalent conductivity change $\Delta\sigma$ (S/m) for Configuration 1 (see Table 5.3). The imaging reconstruction remain the same as in Table 5.1 and only the most significant results are shown.

Table 5.3: Qualitative evaluation of the equivalent conductivity change $\Delta\sigma$ (S/m) recorded in Configuration 1 for different MM parameters. The TSVD is 45 and the CM is *ones(3).*

MM properties		sensitivity	accuracy	area ratio	localization
ε_r (-)	σ (S/m)	(%)	(%)	(-)	error (mm)
20.00	0.30	14.24	92.73	0.14	0.93
50.00	0.10	33.01	94.32	0.33	9.58
35.00	0.50	25.24	93.67	0.25	0.94

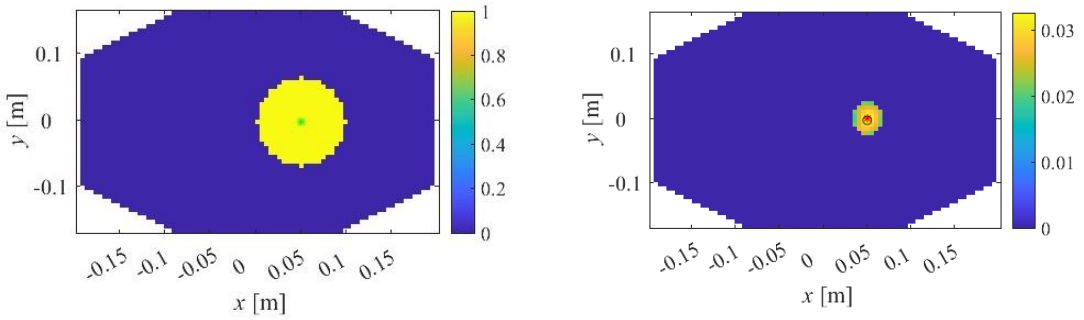

(a) actual binary mask (b) retrieved binary mask + contrast

Figure 5.3: Results of qualitative image evaluation of equivalent conductivity change $\Delta\sigma$ (S/m) in Configuration 1 with MM of ε_r = 20 (-) and σ = 0.3 (S/m), with -3 dB threshold, where the green pixel is actual center of gravity, while the red one is retrieved center of gravity.

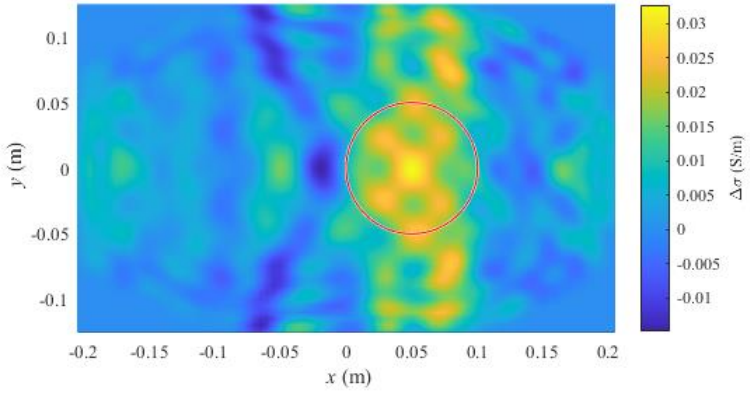

(a) 2-D

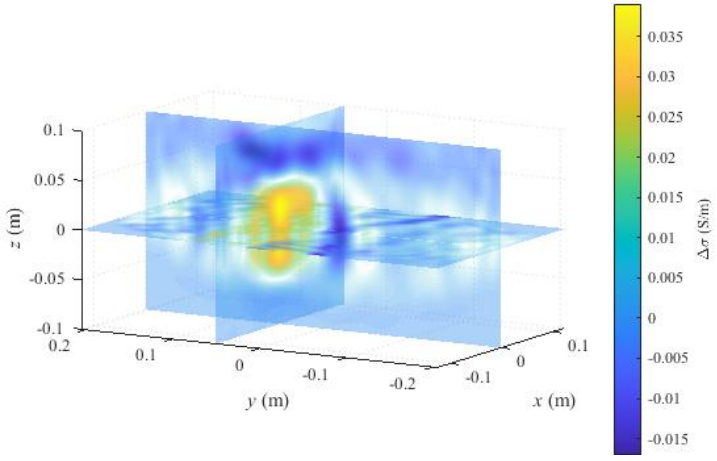

(b) 3-D

Figure 5.4: Image reconstruction of Configuration 1 equivalent conductivity change $\Delta\sigma$ (S/m), for MM with parameters ε_r = 20 (-) and σ = 0.3 (S/m). The TSVD is 45 and the CM is *ones(3)*.

Table 5.4: Quantitative evaluation of the equivalent conductivity change $\Delta\sigma$ (S/m) recorded in Configuration 1 for different MM parameters. The TSVD is 45 and the CM is *ones(3)*.

MM properties		$\Delta\ \sigma$ in the heated	quantitative	$\Delta\ \sigma$ outside the
ε_r (-)	σ (S/m)	area (S/m)	error $\lvert\delta\rvert$ (%)	heated area (S/m)
35.000	0.500	0.016	79.295	0.003
50.000	0.100	0.017	77.716	0.002
20.000	0.300	0.020	74.026	0.004

5.2 Configuration 2

Using 24 UWB antennas in a configuration of two planes, was with the purpose of gaining valuable information about the volume of the cylinder being imaged. As stated in Chapter 2.1, unfortunately MATLAB has a limitation in terms of 3-D imaging where we can only have two additional perpendicular slices in Z direction. On top of that, a 3-D convolution mask is not supported in MATLAB, therefore the volumetric results are raw. The quantitative and qualitative image evaluation does not include the 3-D dimension so again z-axis is only evaluated at point 0. Due to the sufficient amount of UWB antennas a convolution mask is not used for any of the following reconstructions. The TSVD for this model (Configuration 2) is set to 300 following the formula stated in Chapter 5.1.

5.2.1 Relative permittivity evaluation of Configuration 2

Table 5.5: Qualitative evaluation of the total permittivity change $\Delta\varepsilon_r$ (-) for Configuration 2 using a threshold of -3 dB and different matching mediums.

MM properties		sensitivity	accuracy	area ratio	localization
ε_r (-)	σ (S/m)	(%)	(%)	(-)	error (mm)
50.00	0.10	84.14	98.60	0.85	0.74
10.00	0.30	22.99	93.36	0.24	15.18
25.00	0.10	65.70	97.09	0.66	0.78

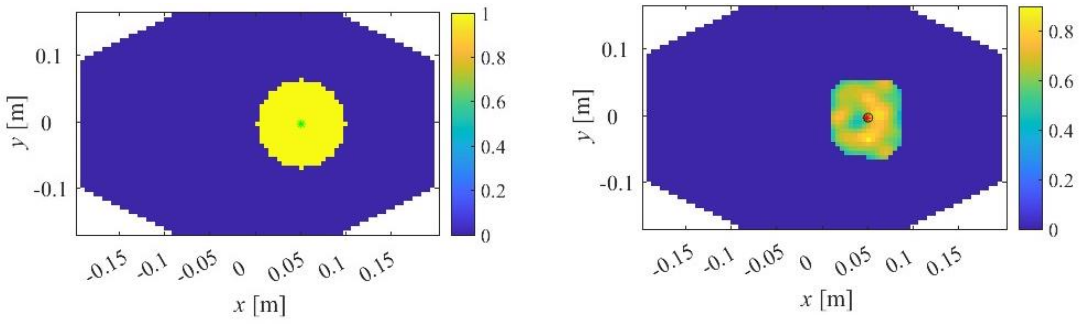

(a) actual binary mask (b) retrieved binary mask + contrast

Figure 5.5: Results of qualitative image evaluation of total permittivity change $\Delta\varepsilon_r$ (-) in Configuration 2 with MM of ε_r = 50 (-) and σ = 0.1 (S/m), with -3 dB threshold, where the green pixel is actual center of gravity, while the red one is retrieved center of gravity.

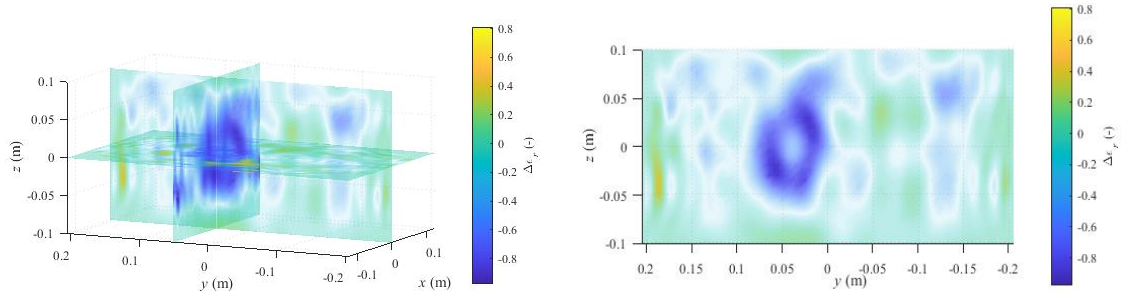

(a) 3-D

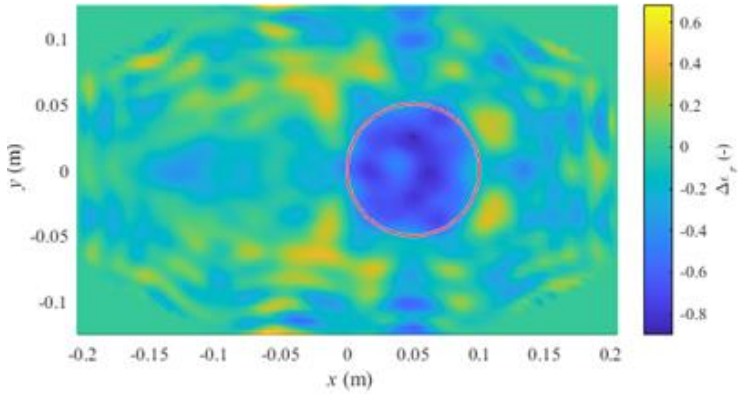

(b) 2-D

Figure 5.6: Image reconstruction of Configuration 2 total permittivity change $\Delta\varepsilon_r$ (-), for MM with parameters ε_r = 50 (-) and σ = 0.1 (S/m). The TSVD is 300 and no CM is applied.

Table 5.6: Quantitative evaluation of the total permittivity change $\Delta\varepsilon_r$ (-) of Configuration 2 for different MM parameters.

MM properties		$\Delta\ \varepsilon_r$ in the	quantitative	$\Delta\ \varepsilon_r$ outside the
ε_r (-)	σ (S/m)	heated area (-)	error $\lvert\delta\rvert$ (%)	heated area (-)
50.00	0.10	-0.61	47.58	-0.06
25.00	0.10	-0.62	46.36	-0.04
10.00	0.30	-0.50	57.08	-0.04

5.2.2 Equivalent conductivity evaluation of Configuration 2

Table 5.7: Qualitative evaluation of the equivalent conductivity change $\Delta\sigma$ (S/m) recorded in Configuration 2 for different MM parameters.

MM properties		sensitivity	accuracy	area ratio	localization
ε_r (-)	σ (S/m)	(%)	(%)	(-)	error (mm)
50.00	0.10	25.24	93.67	0.25	9.19
10.00	0.30	48.22	95.61	0.48	2.83
25.00	0.10	71.84	97.61	0.72	2.45

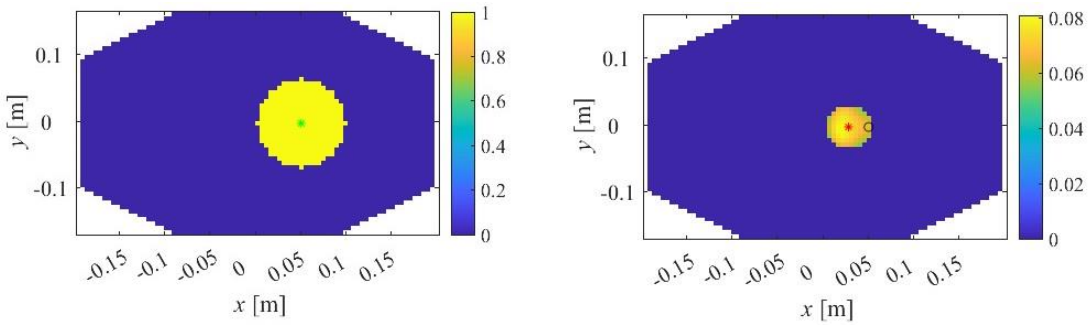

(a) actual binary mask (b) retrieved binary mask + contrast

Figure 5.7: Results of qualitative image evaluation of equivalent conductivity change $\Delta\sigma$ (S/m) in Configuration 2 with MM of ε_r = 50 (-) and σ = 0.1 (S/m), with -3 dB threshold, where the green pixel is actual center of gravity, while the red one is retrieved center of gravity.

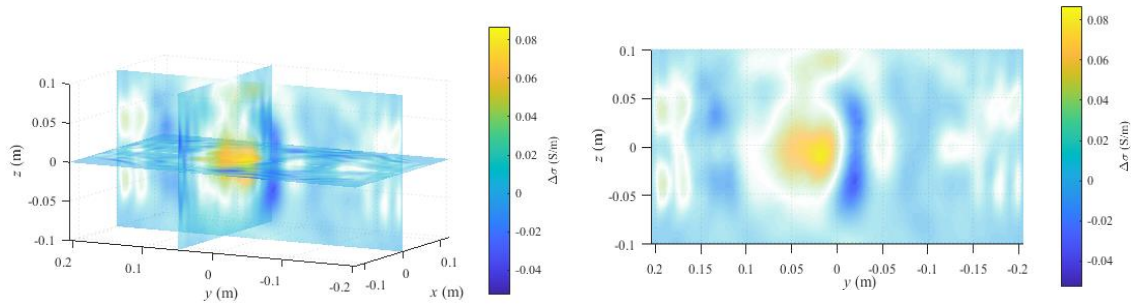

(a) 3-D

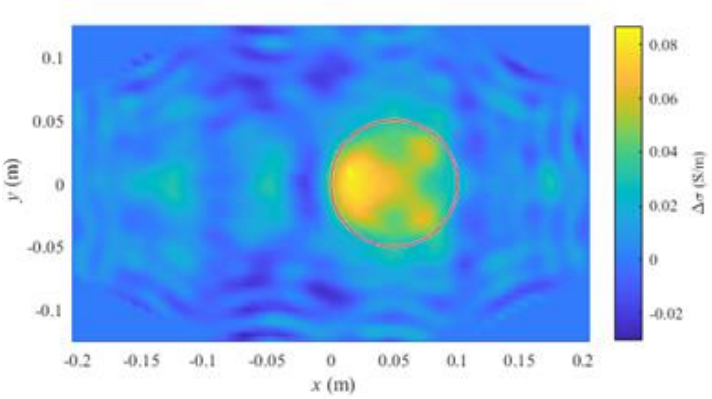

(b) 2-D

Figure 5.8: Image reconstruction of Configuration 2 equivalent conductivity change $\Delta\sigma$ (S/m), for MM with parameters ε_r = 50 (-) and σ = 0.1 (S/m). The TSVD is 300 and no CM is applied.

Table 5.8: Quantitative evaluation of the equivalent conductivity change $\Delta\sigma$ (S/m) recorded in Configuration 2 for different MM parameters.

MM properties		$\Delta\sigma$ in the heated area (S/m)	quantitative error $\lvert\delta\rvert$ (%)	$\Delta\sigma$ outside the heated area (S/m)
ε_r (-)	σ (S/m)			
50.000	0.100	0.051	32.452	0.004
25.000	0.100	0.049	34.608	0.005
10.000	0.300	0.052	31.139	0.005

5.3 Configuration 3

The final geometry presented in this study aims to maximize the 2-D resolution, since it was established that the imaging algorithm currently used in MATLAB is not sufficient for more volumetric information. As follows by the equation in Chapter 5.1 a TSVD of 200 was used an no CM was applied since there is minimal artefacts. With respect to the knowledge gained in Chapters 5.1 and 5.2 the matching liquids investigated are the most suitable, currently for MWI in the pelvic region. Since the results show significantly higher SNR than the models presented in Chapter 5.1 and 5.2, the thresholding was reduced to -6 dB, whiles the size of the disk used for morphologic opening had its radius lowered to 3 pixels. By reducing the image processing the values are approximated better to the experimental.

5.3.1 Relative permittivity evaluation of Configuration 3

Table 5.9: Qualitative evaluation of the total permittivity change $\Delta\varepsilon_r$ (-) for Configuration 3 using a threshold of -6 dB and different matching mediums.

MM properties		sensitivity	accuracy	area ratio	localization
ε_r (-)	σ (S/m)	(%)	(%)	(-)	error (mm)
25.00	0.80	54.37	96.13	0.54	3.11
10.00	1.00	81.55	98.44	0.82	0.62
10.00	0.20	86.08	98.82	0.86	0.13

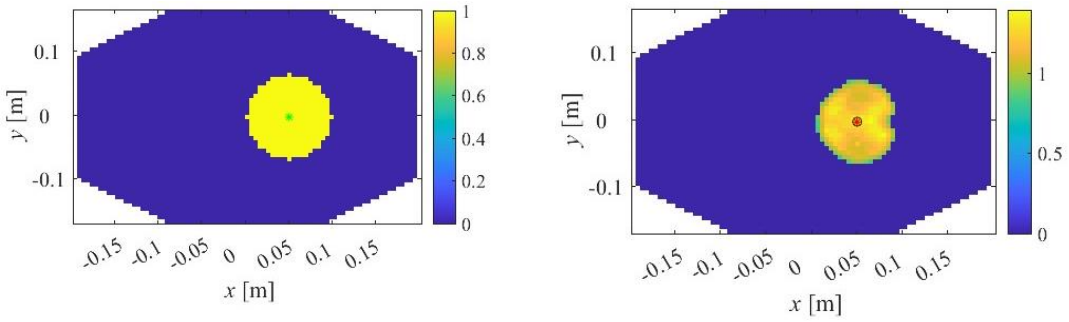

(a) actual binary mask (b) retrieved binary mask + contrast

Figure 5.9: Results of qualitative image evaluation of total permittivity change $\Delta\varepsilon_r$ (-) in Configuration 1 with MM of ε_r = 10 (-) and σ = 0.2 (S/m), with -6 dB threshold, where the green pixel is actual center of gravity, while the red one is retrieved center of gravity.

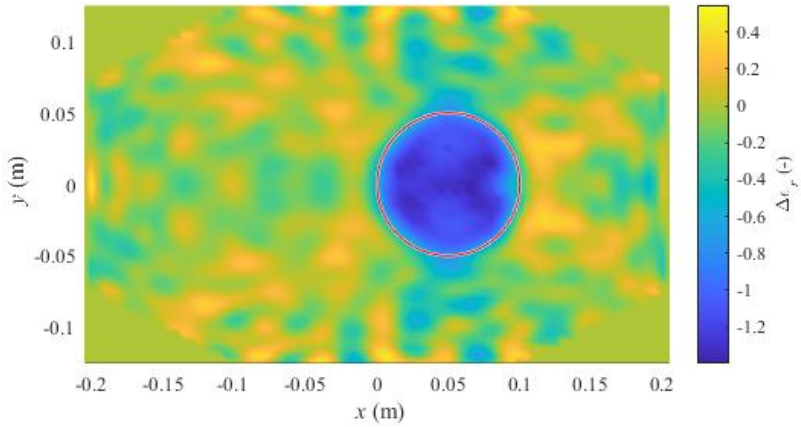

(a) 2-D

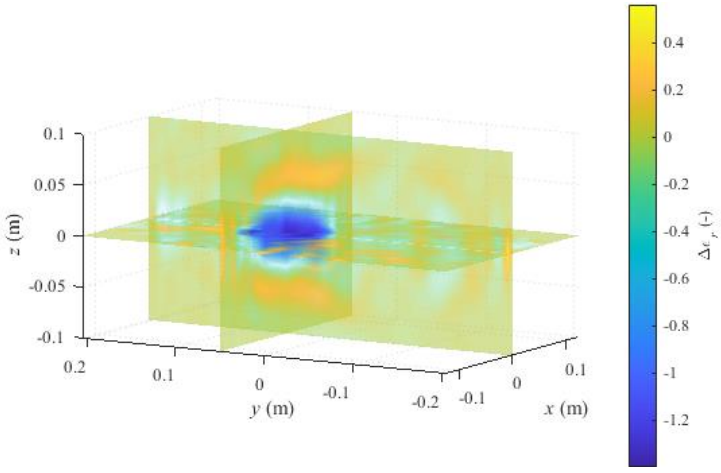

(b) 3-D

Figure 5.10: Image reconstruction of Configuration 3 relative permittivity change $\Delta\ \varepsilon_r$ (-), for MM with parameters ε_r = 10 (-) and σ = 0.2 (S/m). The TSVD is 200 and no CM is applied.

Table 5.10: Quantitative evaluation of the total permittivity change $\Delta\varepsilon_r$ (-) of Configuration 3 for different MM parameters.

MM properties		$\Delta\ \varepsilon_r$ in the heated area (-)	resolution (°C)	quantitative error $\lvert\delta\rvert$ (%)	$\Delta\ \varepsilon_r$ outside the heated area (-)
ε_r (-)	σ (S/m)				
25.00	0.80	-1.00	1.16	13.56	-0.05
10.00	1.00	-1.06	1.09	8.51	-0.05
10.00	0.20	-1.09	1.06	5.50	-0.04

5.3.2 Equivalent conductivity evaluation of Configuration 3

Table 5.11: Qualitative evaluation of the equivalent conductivity change $\Delta\sigma$ (S/m) recorded in Configuration 3 for different MM parameters.

MM properties		sensitivity (%)	accuracy (%)	area ratio (-)	localization error (mm)
ε_r (-)	σ (S/m)				
25.00	0.80	74.11	97.64	0.76	1.48
10.00	1.00	62.78	96.68	0.65	1.81
10.00	0.20	90.29	98.22	1.02	0.44

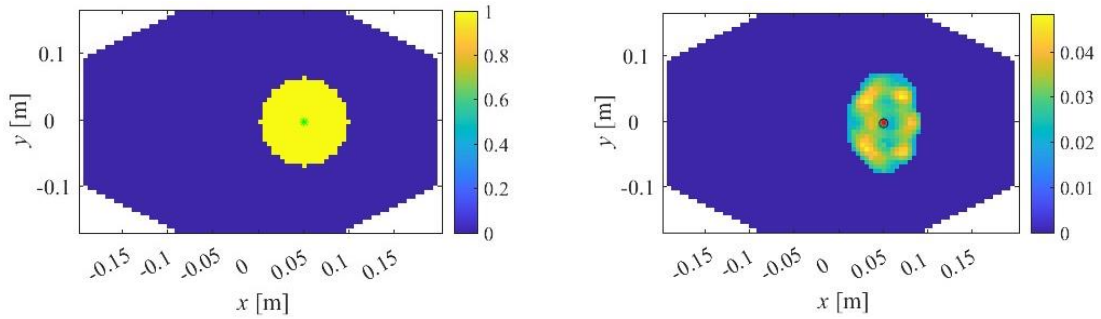

(a) actual binary mask (b) retrieved binary mask + contrast

Figure 5.11: Results of qualitative image evaluation of equivalent conductivity change $\Delta\sigma$ (S/m) in Configuration 3 with MM of ε_r =10 (-) and σ = 0.2 (S/m), with -6 dB threshold, where the green pixel is actual center of gravity, while the red one is retrieved center of gravity.

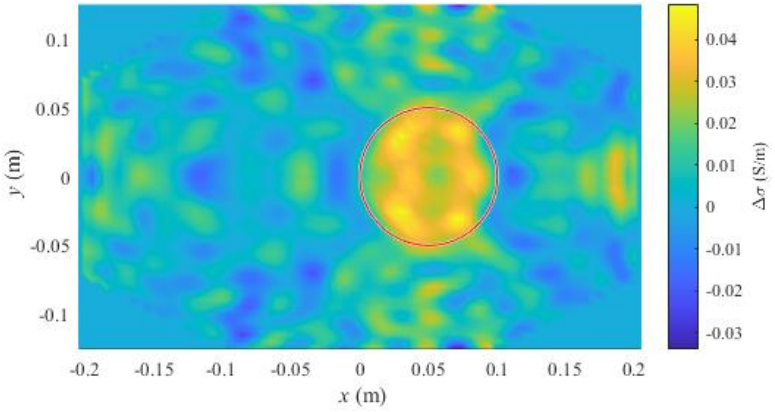

(a) 2-D

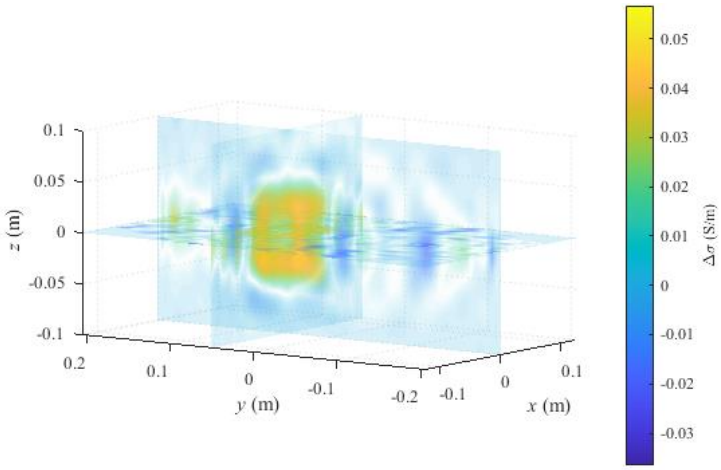

(b) 3-D

Figure 5.12: Image reconstruction of Configuration 3 equivalent conductivity change $\Delta\sigma$ (S/m), for MM with parameters ε_r =10 (-) and σ = 0.2 (S/m). The TSVD is 200 and no CM is applied.

Table 5.12: Quantitative evaluation of the equivalent conductivity change $\Delta\sigma$ (S/m) recorded in Configuration 3 for different MM parameters.

MM properties		$\Delta\sigma$ in the heated area (S/m)	resolution (°C)	quantitative error $\lvert\delta\rvert$ (%)	$\Delta\sigma$ outside the heated area (S/m)
ε_r (-)	σ (S/m)				
25.000	0.800	0.030	2.482	59.714	0.003
10.000	1.000	0.033	2.309	56.682	0.004
10.000	0.200	0.030	2.506	60.091	0.004

5.4 Numerical model reconstructions with noise

To further prove the feasibility of the numerical models presented in Chapter 5.3, noise is introduced to the reconstructions to assess its effect. Since noise is inevitable in the experimental setup its impact has to be studied and predicted to maximize the quality of the produced outputs. The main goal of the section is to find the highest noise that can be in the environment and not significantly affect the performance of the numerical simulations.

Configuration 3 with 22 UWB antennas and a MM with parameters ε_r = 10 (-) and σ = 0.2 (S/m) performed the best out of all numerical models with a quantitative error of 5.5 % and 98.2 % accuracy, therefore the introduction of noise was performed and evaluated only on it. The five levels of noise added were 110dB, 100 dB, 90 dB, 80 dB and 70 dB. Only the results with significant importance are to be presented in this section, since the changes in small steps are not visible. The rest can be found in Appendix B. Firstly, are presented the S-matrix and the differential module of the matrices. The changes in the phases will not be presented in this paper due to the fact that they are minimal because of the simplicity of the phantom geometry. For investigation of more complex phantom geometries, they must also be studied. The main point of focus is in the changes of the useful signal in the S-matrices and how the introduced noise can mask it. Following that are presented the analogical reconstructions with the Born Approximation with truncated singular value decomposition (TSVD), such as in Chapter 5.3. The TSVD number is decreased with the increasing of the noise to avoid reconstruction of too much noise. Because of that for each noise level the most fitting TSVD is also specified.

A convolution mask of *ones(3)* is applied to all presented reconstructions in this section. Although image post-processing is not a part of this thesis, the reconstructions achieved will also be presented with additional re-processing further in this section. The changes in the results are extremely insignificant up to the 90 dB noise level and completely masked by the noise below 80 dB. Because of that only the comparison between no added noise, 90 dB and 80 dB is shown.

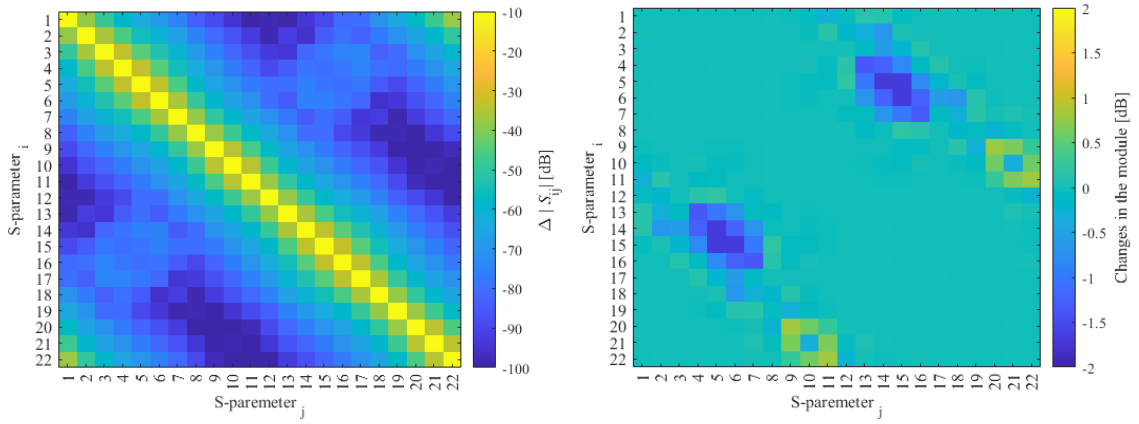

(a) No noise

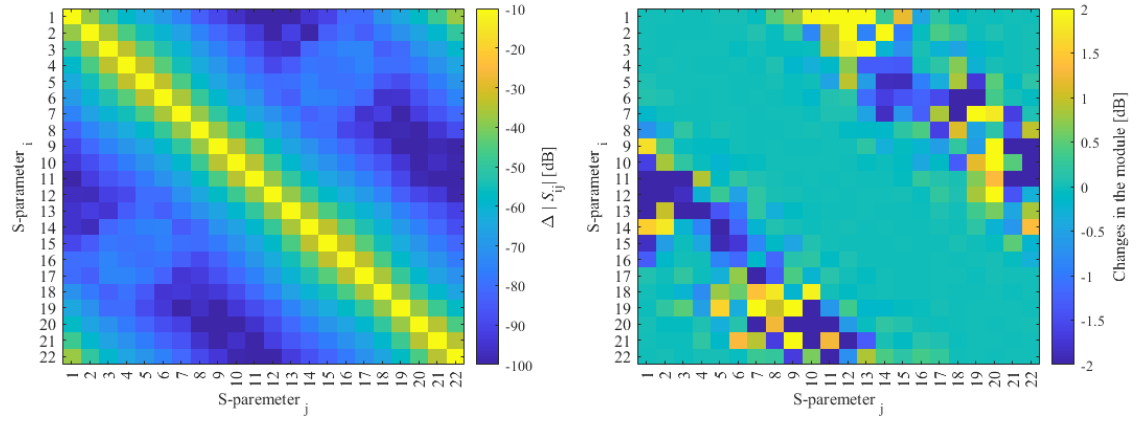

(b) 90 dB noise

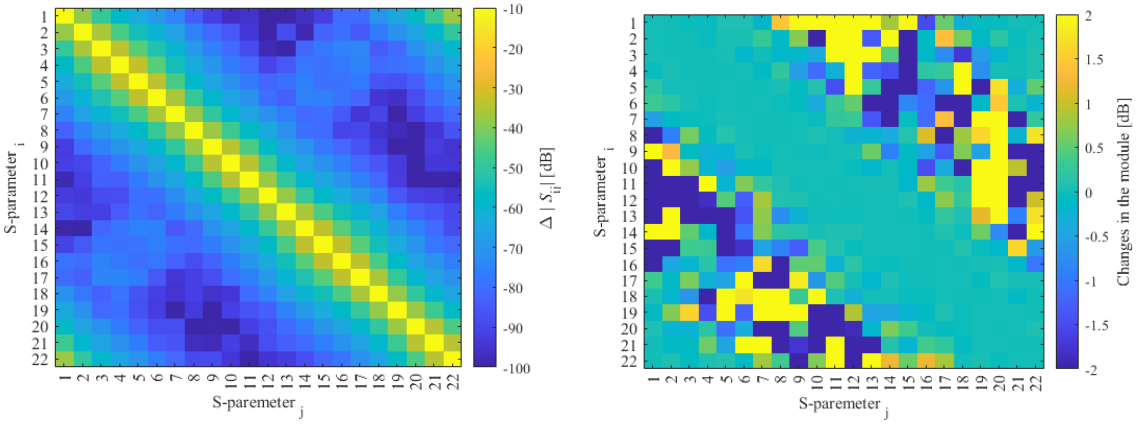

(c) 80 dB noise

Figure 5.13: Scattering matrix and differential module matrix of Configuration 3 with a matching medium ε_r = 10 (-) and σ = 0.2 (S/m). No noise – (a), 90 dB noise – (b), 80 dB noise – (c).

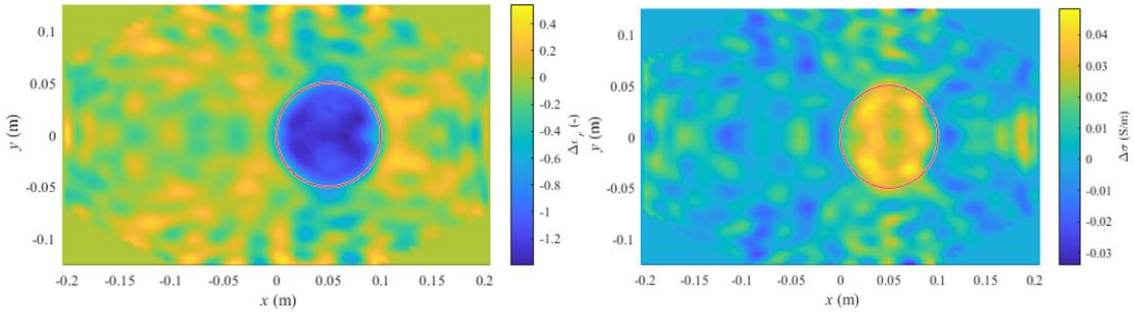

(a) No noise

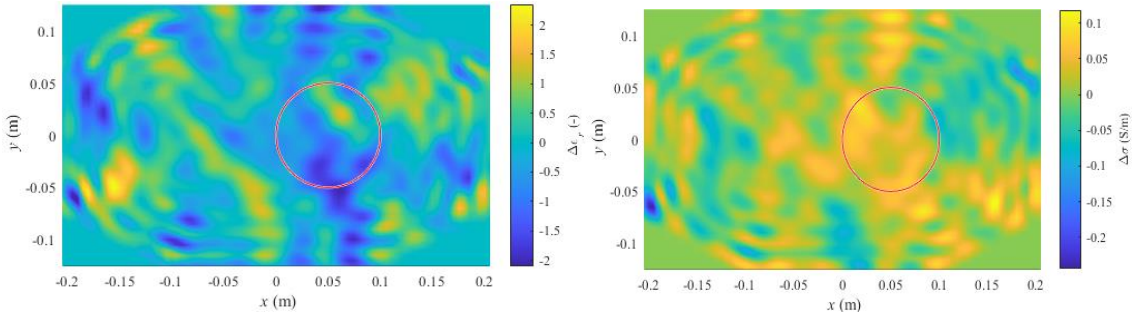

(b) 90 dB noise

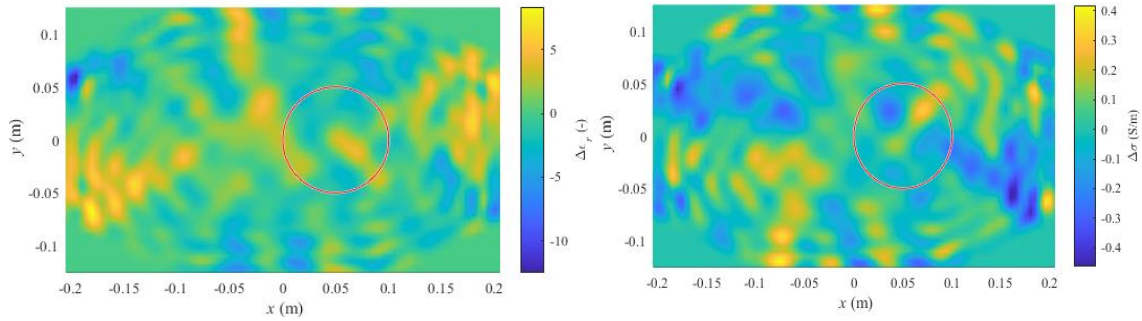

(c) 80 dB noise

Figure 5.14: Reconstructions of the change in relative permittivity $\Delta\varepsilon_r$ (-) and equivalent conductivity change $\Delta\sigma$ (S/m) of Configuration 3 with a matching medium $\varepsilon_r = 10$ (-) and $\sigma = 0.2$ (S/m). No noise: TSVD = 200 – (a), 90 dB noise: TSVD = 40 – (b), 80 dB noise: TSVD = 35 – (c)

The reconstructions with added noise below 100 dB are not sufficient for any monitoring purpose. For this reason, again was investigated the influence of the matching medium of the numerical model. After further testing another MM was proposed, which improved the results significantly: $\varepsilon_r = 40$ (-) and $\sigma = 0.7$ (S/m).

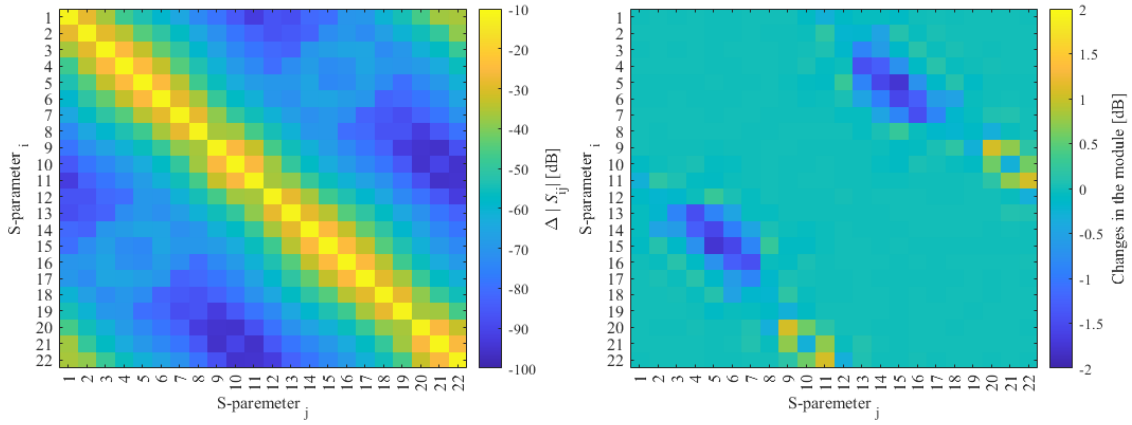

(a) No noise

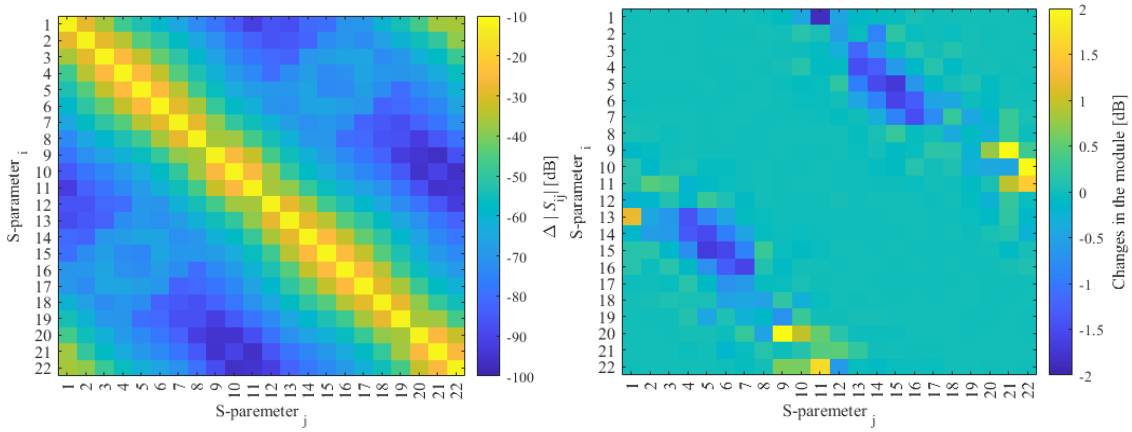

(b) 90 dB noise

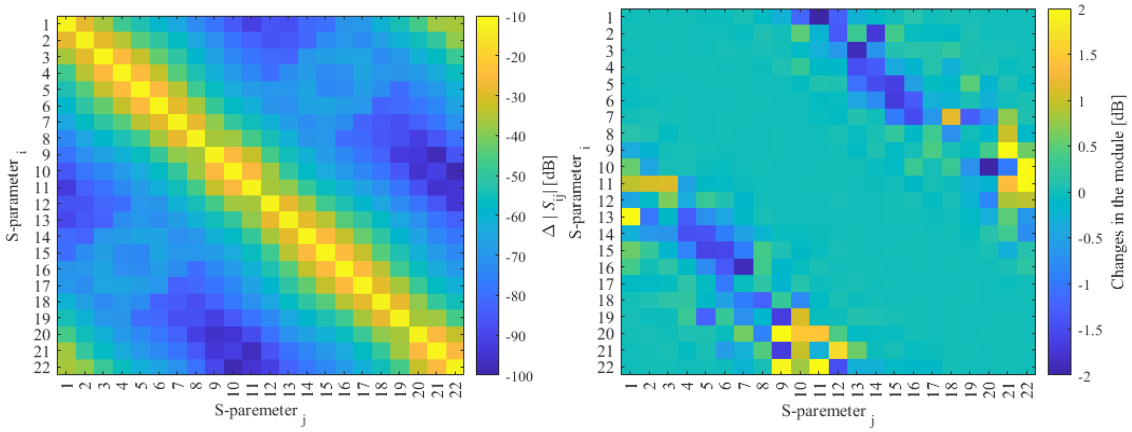

(c) 80 dB noise

Figure 5.15: Scattering matrix and differential module matrix of Configuration 3 with a matching medium ε_r = 40 (-) and σ = 0.7 (S/m). No noise – (a), 90 dB noise – (b), 80 dB noise – (c).

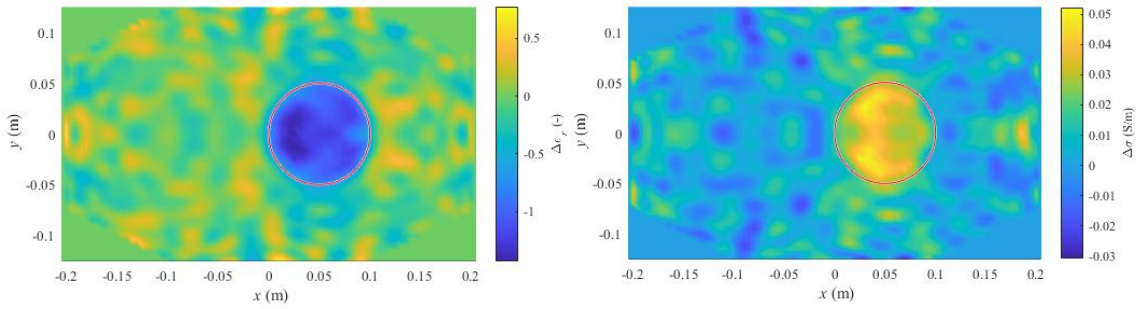

(a) No noise

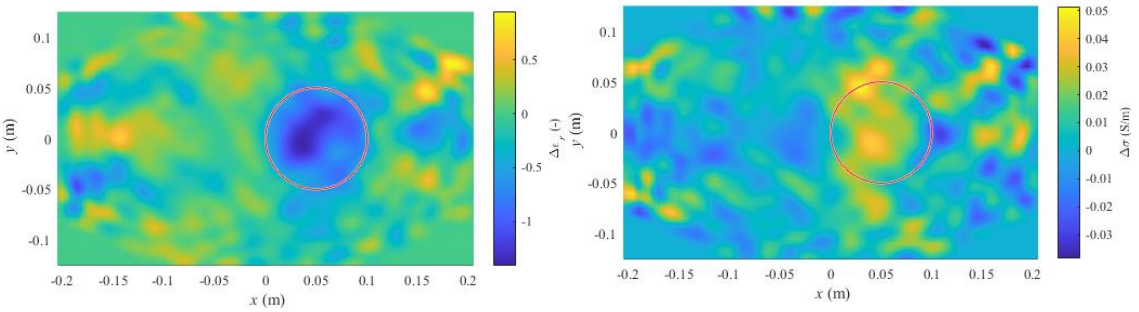

(b) 90 dB noise

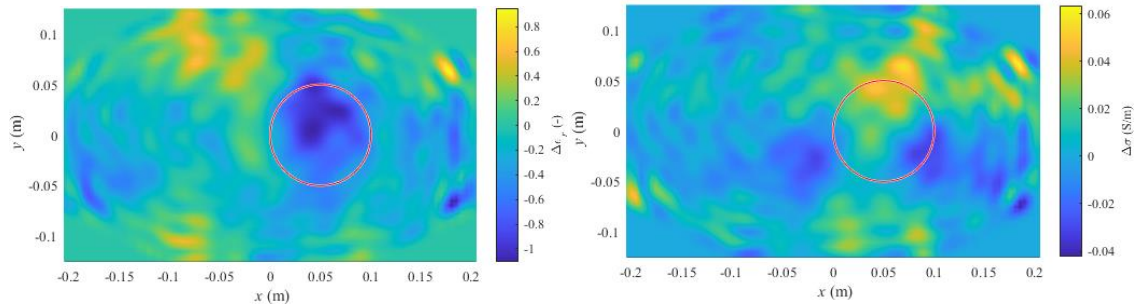

(c) 80 dB noise

Figure 5.16: Reconstructions of the change in relative permittivity $\Delta\varepsilon_r$ (-) and equivalent conductivity change $\Delta\sigma$ (S/m) of Configuration 3 with a matching medium $\varepsilon_r = 40$ (-) and $\sigma = 0.7$ (S/m). No noise: TSVD = 200 – (a), 90 dB noise: TSVD = 80 – (b), 80 dB noise: TSVD = 33 – (c)

The following tables represent the qualitative and quantitative assessment of the reconstructions presented in Figure 5.16. The method of obtaining these values is the same as in Chapter 5.3 and is described in Chapter 4.4.

Table 5.13: Qualitative evaluation of the relative permittivity change $\Delta\varepsilon_r$ (-) reconstructed from Configuration 3 for three levels of noise. A standard thresholding of -3 dB is applied.

noise level (dB)	sensitivity (%)	specificity (%)	accuracy (%)	area ratio (-)	localization error (mm)
0	77.70	100.00	98.11	0.78	0.82
90	57.28	100.00	96.38	0.57	1.94
80	83.17	98.98	97.64	0.94	1.40

Table 5.14: Qualitative evaluation of the equivalent conductivity change $\Delta\sigma$ (S/m) reconstructed from Configuration 3 for three levels of noise. A standard thresholding of -3 dB is applied.

noise level (dB)	sensitivity (%)	specificity (%)	accuracy (%)	area ratio (-)	localization error (mm)
0	58.58	100.00	96.49	0.59	2.42
90	26.54	100.00	93.78	0.27	3.48
80	11.97	98.65	91.31	0.27	19.77

Table 5.15: Quantitative evaluation of the relative permittivity change $\Delta\varepsilon_r$ (-) reconstructed from Configuration 3 for three levels of noise. A standard thresholding of -3 dB is applied.

noise level (dB)	$\Delta\ \varepsilon_r$ in the heated area (-)	resolution (°C)	quantitative error $\lvert\delta\rvert$ (%)	$\Delta\ \varepsilon_r$ outside the heated area (-)
0	-1.04	1.11	9.60	-0.04
90	-0.87	1.33	24.76	-0.05
80	-0.74	1.55	35.67	-0.09

Table 5.16: Quantitative evaluation of the equivalent conductivity change $\Delta\sigma$ (S/m) reconstructed from Configuration 3 for three levels of noise. A standard thresholding of -3 dB is applied.

noise level (dB)	$\Delta\sigma$ in the heated area (S/m)	resolution (°C)	quantitative error $\|\delta\|$ (%)	$\Delta\sigma$ outside the heated area (S/m)
0	0.032	2.367	57.759	0.004
90	0.020	3.715	73.080	0.004
80	0.012	6.210	83.898	0.003

In the following figures, as stated before are suggested some image post-processing tools. In Figure 5.17 can be seen a proposed Gaussian convolution kernel and next in Figure 5.18 is made a comparison between a simple convolution mask and a combination of the kernel with median filtering (*medfilt2*) tool provided by MATLAB.

```
A =

     1     1    -2     1     1
     1    -2     9    -2     1
    -2     9     9     9    -2
     1    -2     9    -2     1
     1     1    -2     1     1
```

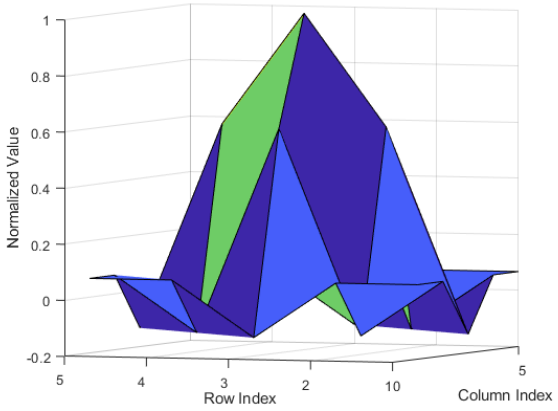

Figure 5.17: Proposed 5x5 convolution kernel for noise reduction image post-processing.

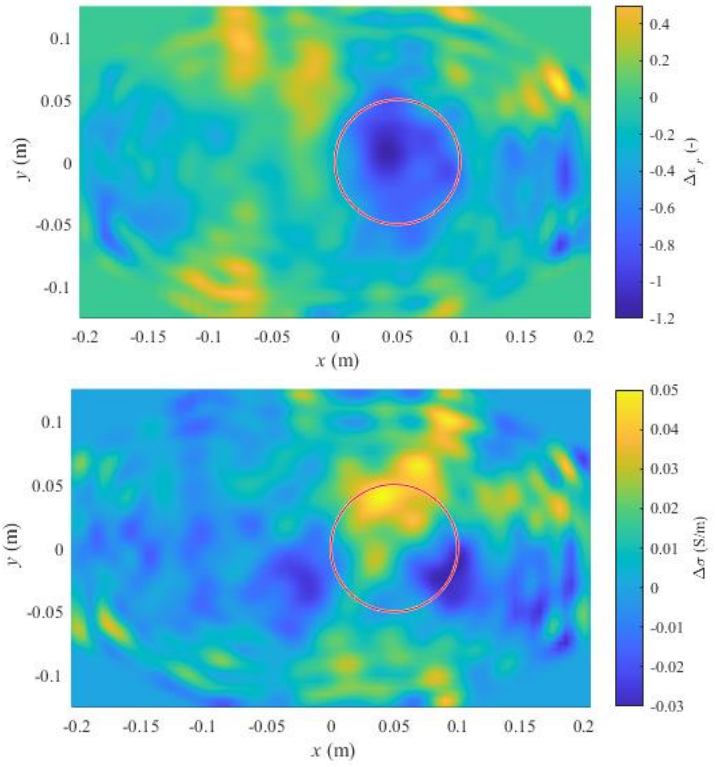

(a) convolution mask *ones(3)*

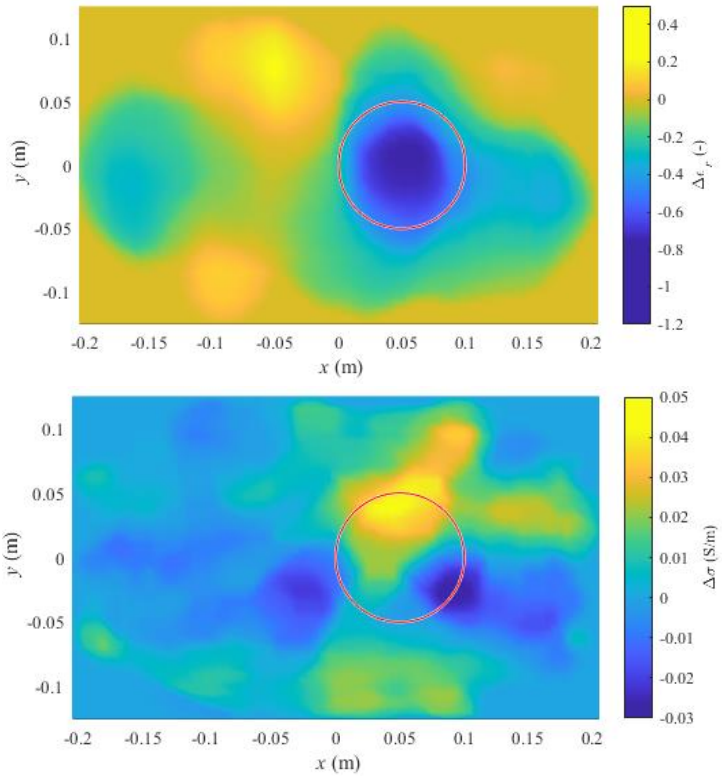

(b) Gaussian convolution mask + median filtering

Figure 5.18: Comparison of reconstruction with a regular convolution mask (a) and Gaussian convolution kernel (see Figure 5.17) with median filtering (b).

5.5 Experiment

5.5.1 Reflection coefficient measurements

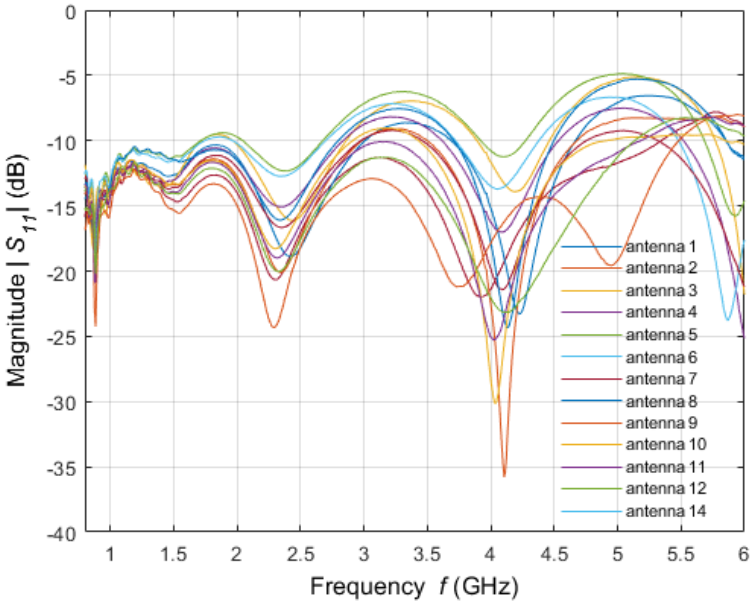

(a) antenna # 1-13

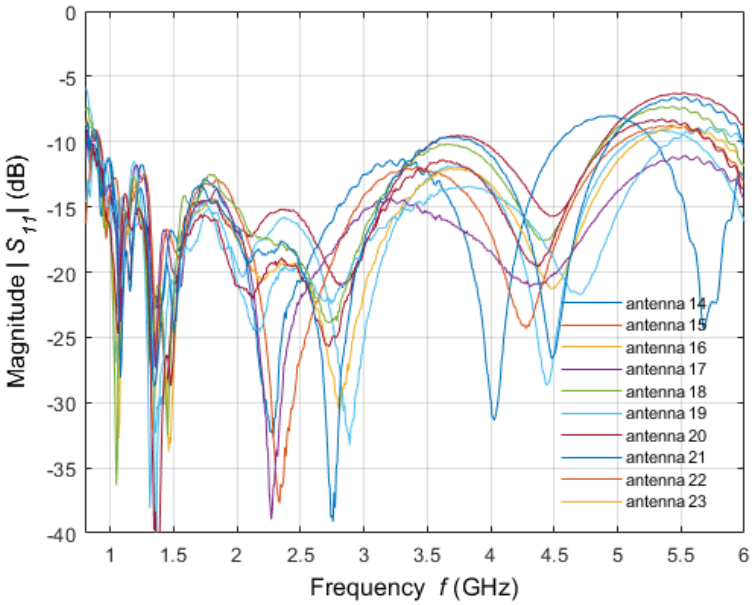

(b) antenna # 14 - 23

Figure 5.19: Comparison of reflection coefficient $|S_{11}|$ (dB) of 23 UWB antennas in contact with distilled water in the range of 0.8 - 6 GHz.

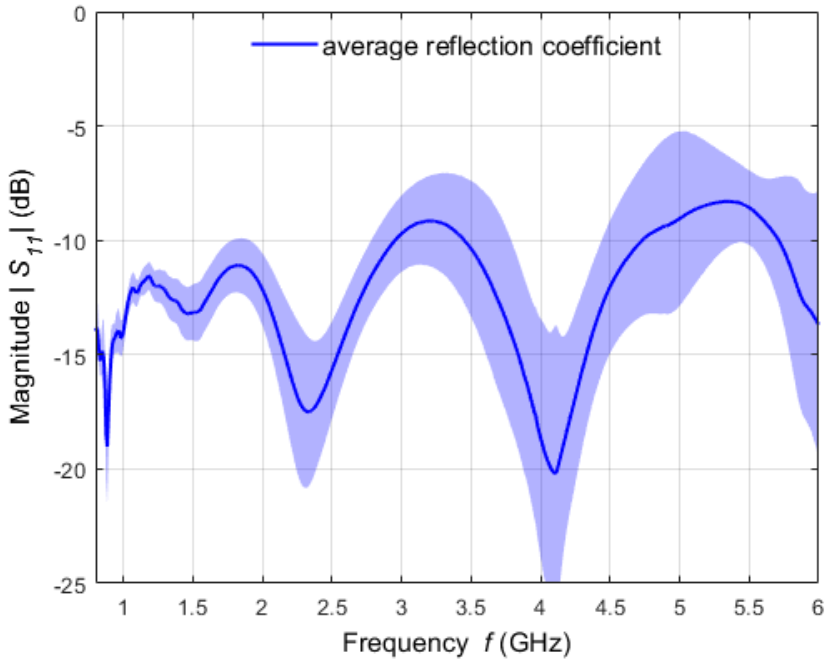

(a) antenna # 1-13

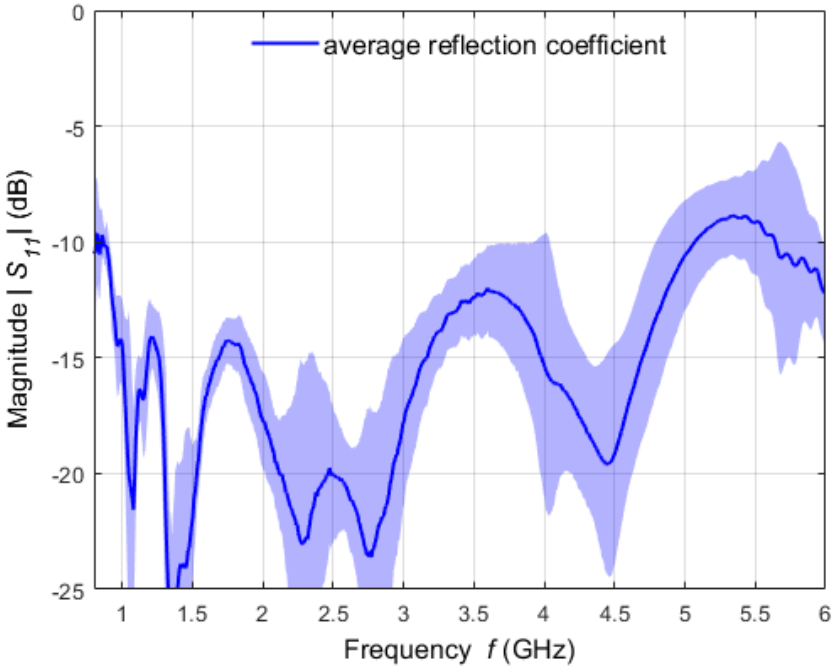

(b) antenna # 14 - 23

Figure 5.20: Average reflection coefficient $|S_{11}|$ (dB) of 23 UWB antennas in contact with distilled water in the range of 0.8 - 6 GHz and standard deviation.

5.5.2 Muscle liquid phantom

Table 5.17: Measured dielectric properties of two muscle liquid phantoms representing temperatures of 37 °C and 45 °C at frequency of 1 GHz including their uncertainties.

Phantom	37 °C		45 °C	
Properties	Permittivity (-)	Conductivity (S/m)	Permittivity (-)	Conductivity (S/m)
Value	55.732	0.707	52.754	0.799
Uncertainty type A	0.553	0.012	0.027	0.001
Uncertainty type B	0.474	0.010	0.448	0.011
Uncertainty type C	0.728	0.009	0.449	0.004

The target values were the following: for 37 °C, ε_r = 54.21 (-) and σ = 0.72 (S/m); for 45 °C, ε_r = 53.06 (-) and σ = 0.80 (S/m).

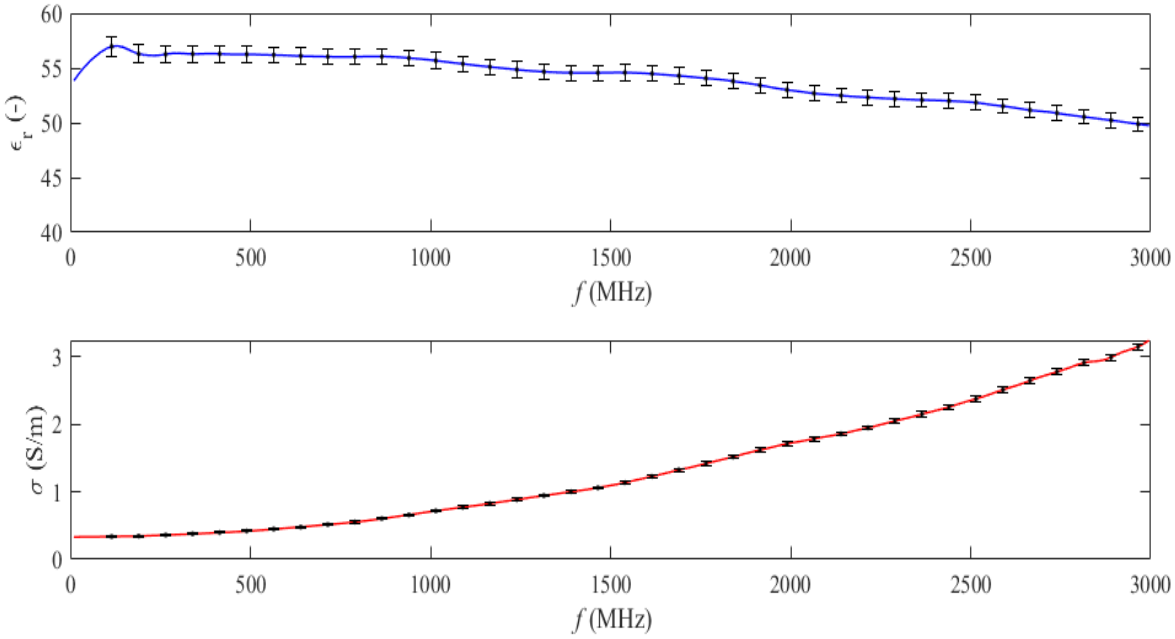

Figure 5.21: Frequency dependency of measured dielectric properties with standard deviation bars of a muscle liquid phantom representing a temperature of 37 °C at 1000 MHz.

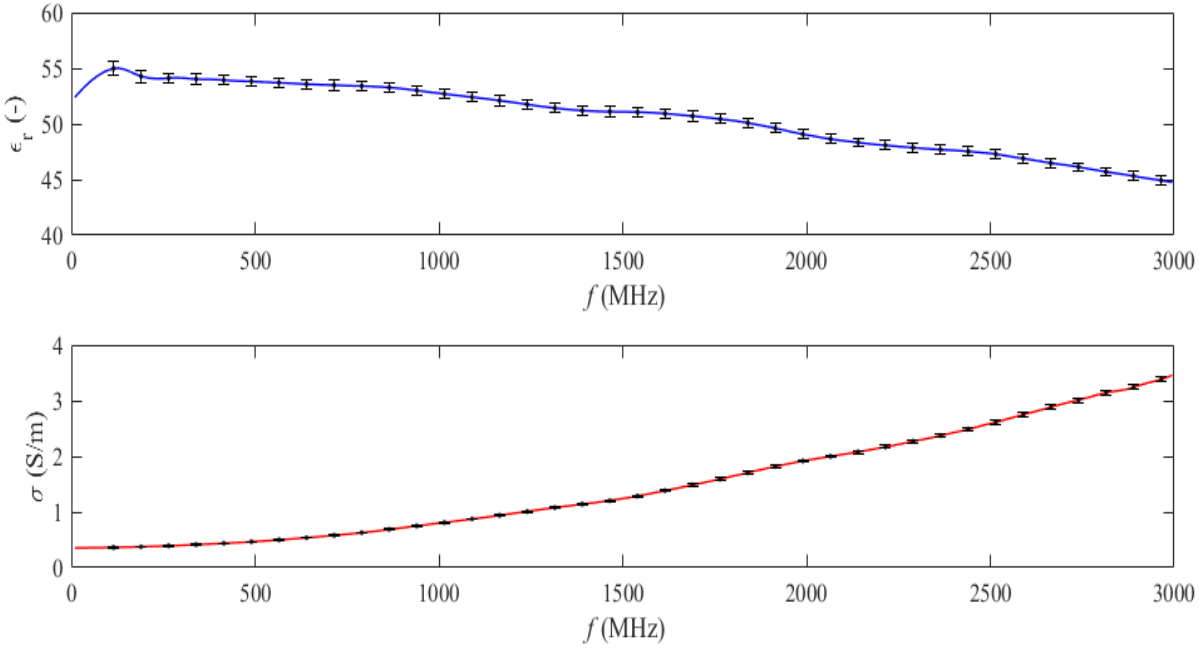

Figure 5.22: Frequency dependency of measured dielectric properties with standard deviation bars of a muscle liquid phantom representing a temperature of 45 °C at 1000 MHz.

5.5.3 Experimental reconstructions

In this section are presented the first reconstructions from the experimental setup. The method of obtaining the results is described in Chapter 4.6.3. In the previous section it was determined that the matching medium with dielectric properties ε_r = 10 (-) and σ = 0.2 (S/m) performs best under perfect conditions, it was also established that it is not at all sufficient for highly noise-affected environment, that is why a new MM was proposed. Unfortunately, the experimental measurement was performed prior to gaining that information that is why in this section only reconstructions with the MM ε_r = 10 (-) and σ = 0.2 (S/m) are presented.

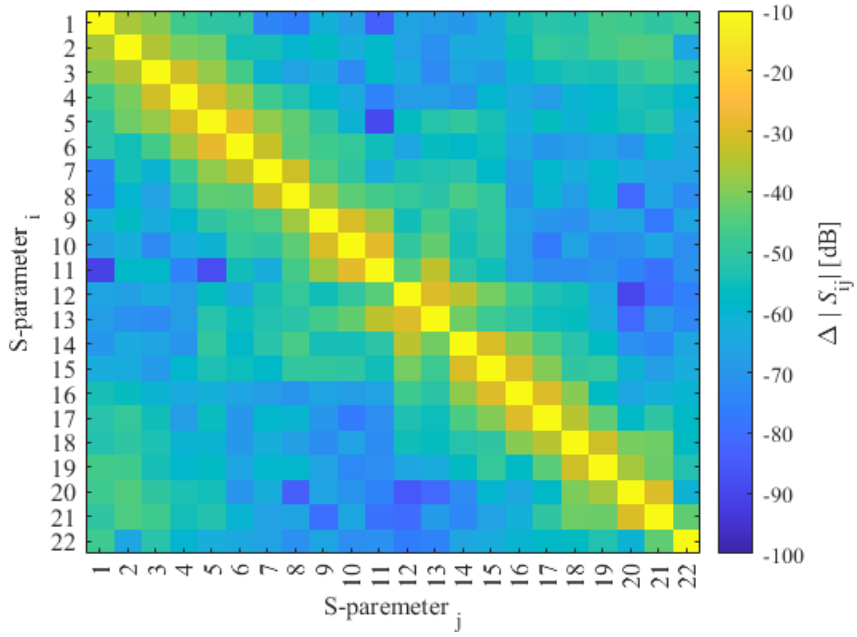

(a)

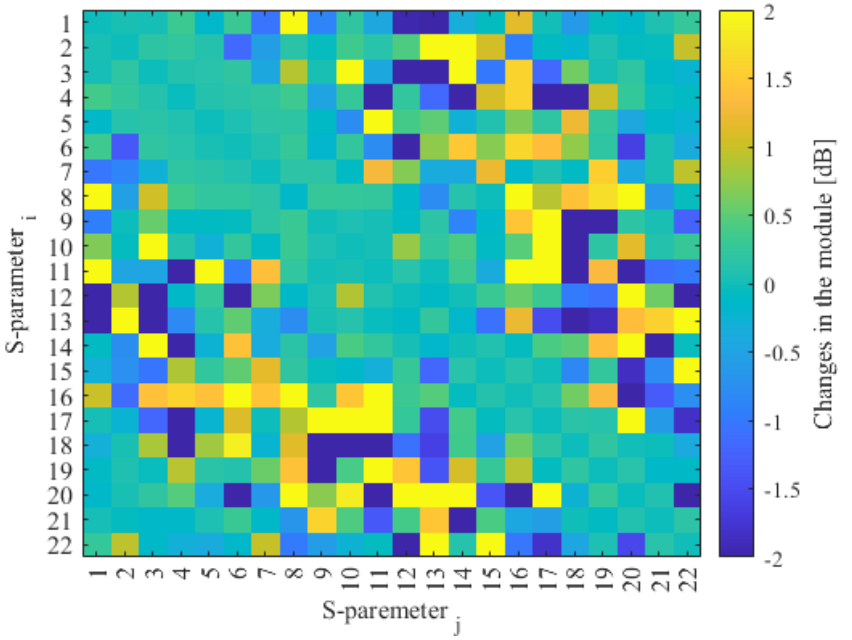

(b)

Figure 5.23: Scattering S-matrix (a) and differential module S-matrix (b) from the first experimental measurement described in Chapter 4.6.3.

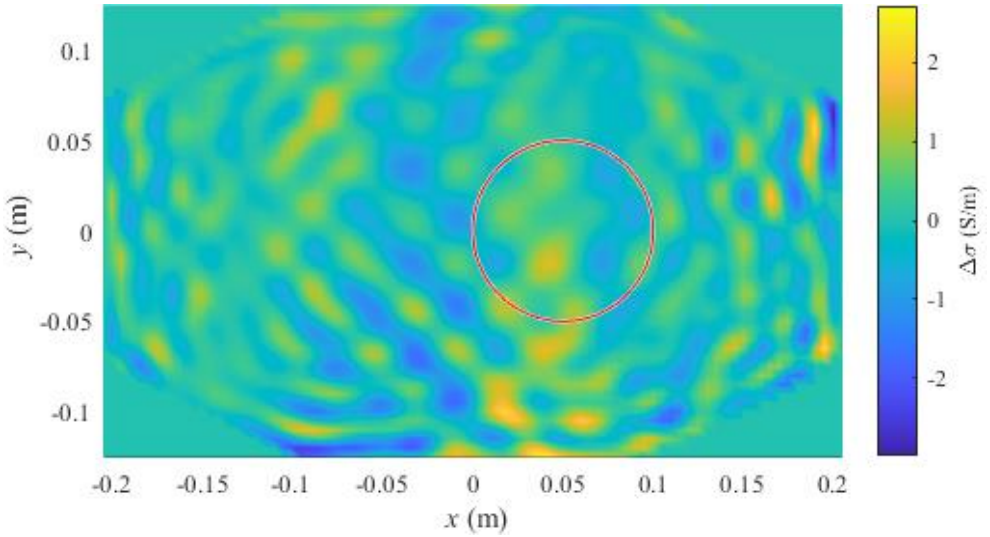

(a) Δ σ (S/m)

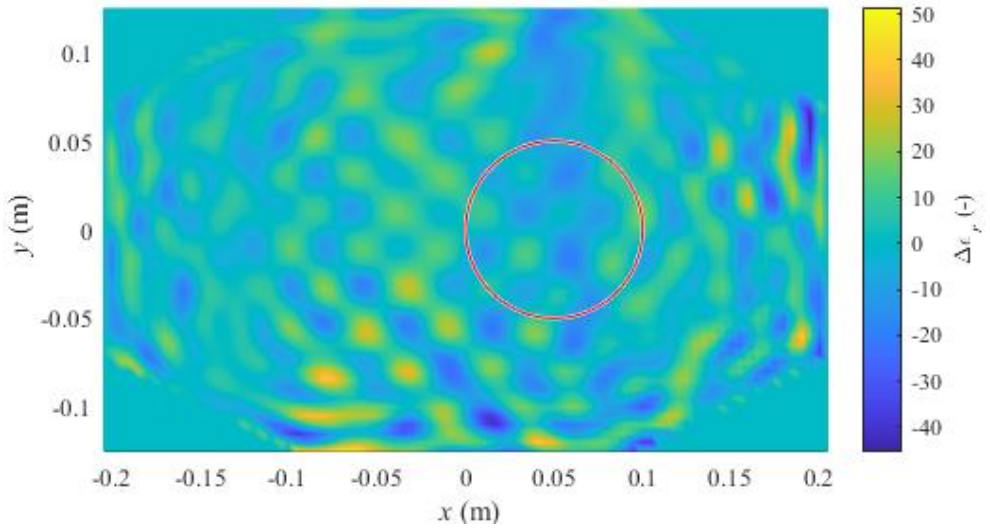

(b) Δ ε_r (-)

Figure 5.24: First contrast reconstructions from experimental measurement for equivalent conductivity changes (a) and relative permittivity changes (b). The TSVD is 18 and a convolution mask *ones(3)* is applied.

For further investigation of why the reconstructions were unsuccessful was measured the noise floor of the system with a matching medium approximating the newly proposed one in the previous section: ε_r = 40 (-) and σ = 0.7 (S/m). On top of that, was used a smaller frequency IF bandpass filter on the VNA of 10 Hz, while for the measurement was used 100 Hz.

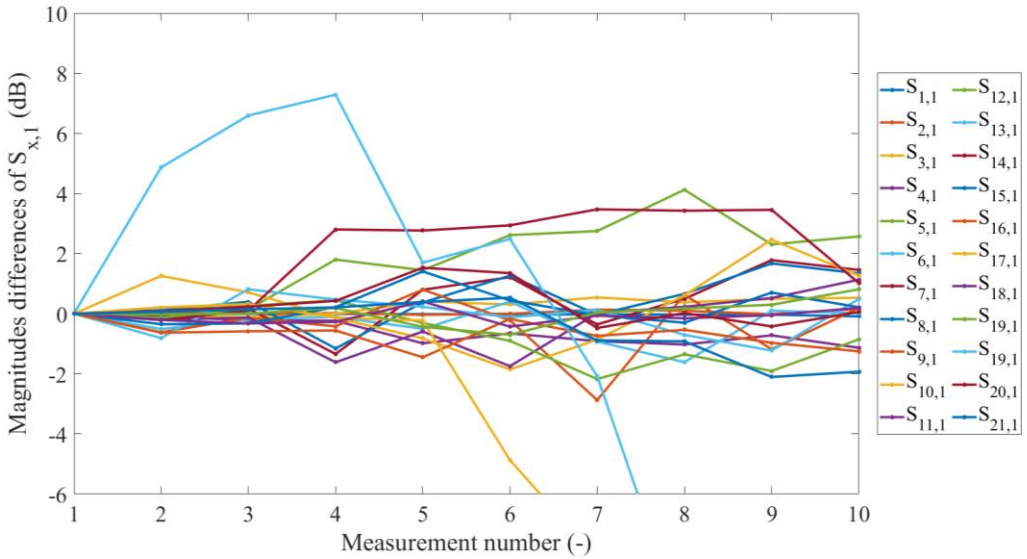

Figure 5.25: Measured change in the transmission coefficients $|S_{ij}|$ (dB) over 10 consecutive measurements of a homogenous muscle liquid phantom with a frequency bandpass filter of 100 Hz.

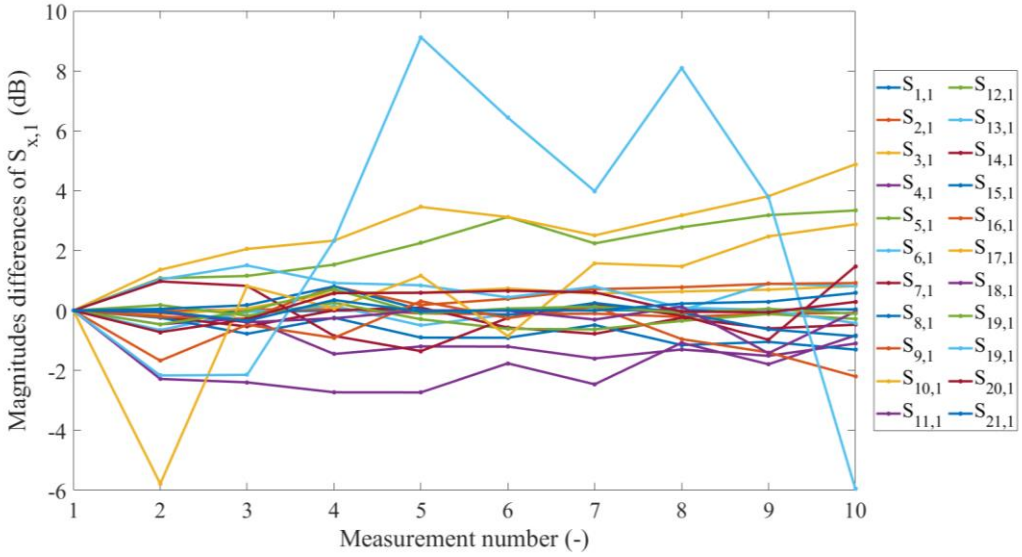

Figure 5.26: Measured change in the transmission coefficients $|S_{ij}|$ (dB) over 10 consecutive measurements of a homogenous muscle liquid phantom with a frequency bandpass filter of 10 Hz.

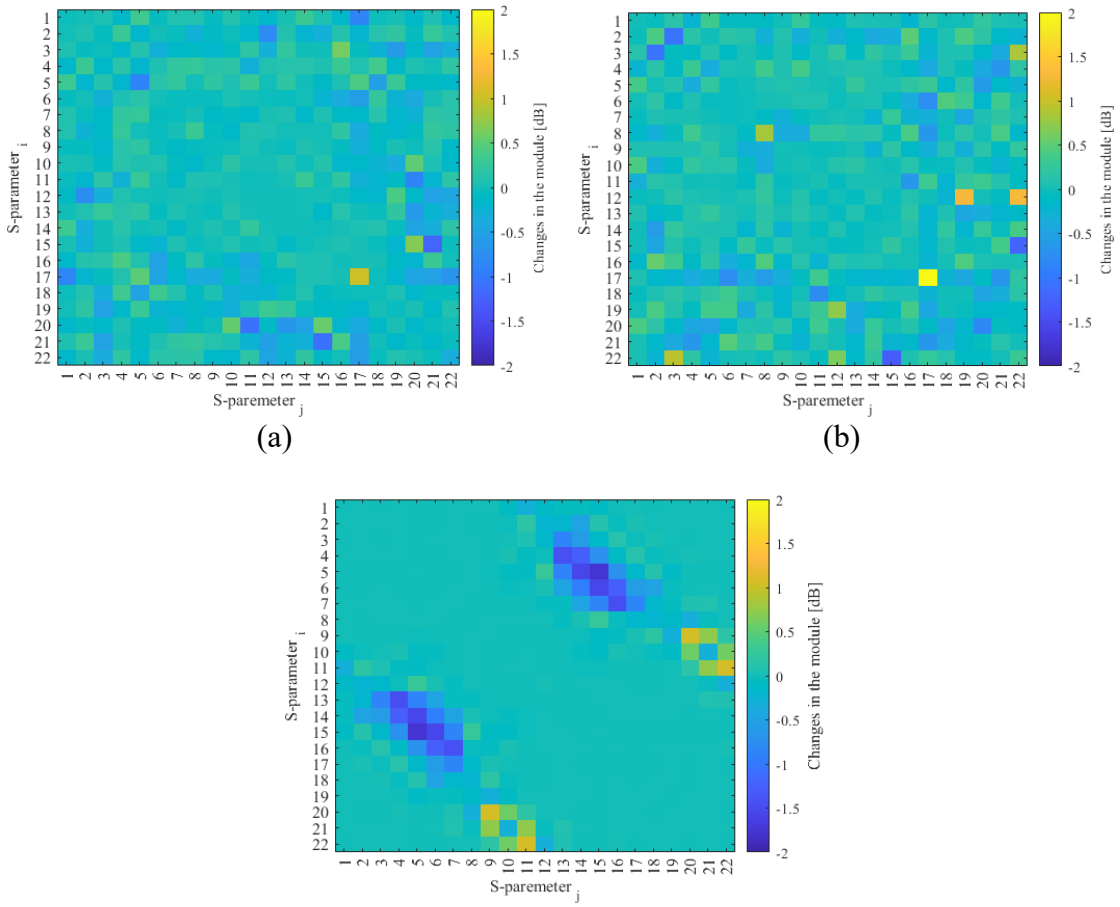

Figure 5.27: Comparison of the changes in module (dB) caused by noise in 10 consecutive measurements with a 100 Hz bandpass IF filter of the VNA - (a), 10 Hz bandpass IF filter of the VNA - (b) and changes in module (dB) caused by the introduction of the heated muscle phantom with no noise from a numerical simulation (c).

Table 5.18: Noise floor measurement of the experimental setup with a MM with dielectric properties ε_r = 40 (-) and σ = 0.7 (S/m). Two IF bandpass filters of the vector network analyser are compared.

IF filter bandpass filter (Hz)	Mean (dB)	standard deviation (dB)
100	-0.0460	± 0.2397
10	-0.0085	± 0.3002

6 Discussion

6.1 Numerical models

The three numerical models created in COMSOL Multiphysics exhibit different behavior. With the increase of the number of the UWB antennas in one plane the quality and quantity of the results in that same slice significantly increases. Therefore, for most optimal experimental study for 2-D temperature imaging at least 22 UWB antennas must be used, as in Configuration 3 (see Figure 4.4). In Configuration 2 (see Figure 4.3) some volumetric information was gained, as seen in Figure 5.6 and Figure 5.8, but with very poor quality and resolution, due to the incapability of MATLAB to do 3-D interpolation and plot volumetric values clearly. On top of that, the antennas were placed directly vertically of each other, resulting in slight mutual coupling due to the propagation of EM field from the bowtie [21,31]. Therefore, in terms of imaging in 3-D, the best results can be achieved by a properly interpolated or diagonal-like configuration of the antennas, for example like in [31], and a different platform for the image reconstruction that would allow for interpolation between slices in z-axis.

The distorted Born approximation (DBA) with truncated singular value decomposition (TSVD) algorithm was used to solve the inverse-scattering problem in the designed numerical models. It provides the best imaging results when the number of antennas is sufficient enough to create large amount normalized singular values. That allows for the minimalization of post-processing, as in Figure 5.10 and Figure 5.12, while the TSVD is kept at a value slightly below the $TSVD_{max}$ (see Formula 5.1). The CM decreases the differences outiside the area of interest providing more homogenous results, but it significantly decreases the resolution in the heated region. As for the TSVD limit used to reconstruct Configuration 3 (Figure 5.10, Figure 5.12), the calculated $TSVD_{max}$ is 231, but the better results of the reconstruction were seen at TSVD = 200, as even numerical simulation softwares like COMSOL Multyphysics introduce some extremly small level of noise-like deviations, hidden in the highest normalized singular values.

The image evaluation of the two parameters, namely relative permittivity ε_r (-) and equivalent conductivity σ (S/m), provide the opportunity to not only study the best matching medium more precisely, but also whether both of them could be used for the

temperature monitoring combined or each separately. The reconstruction evaluation of Configuration 3, with the most suitable MM values stated in Chapter 4.1, in terms of quantity and quality for the relative permittivity, showed a minimal percentage error in the heated area of 5.5 %, a sensitivity of 86.08 %, an accuracy of 98.82 %, an area ratio of 0.86 and localization error of 0.13 mm (Table 5.9 and Table 5.10). The quantitative performance of the equivalent conductivity change $\Delta\sigma$ is poor with a percentage error of 60%. On the other hand, qualitatively the results provide valuable information with sensitivity of 90.29 %, accuracy of 98.22 %, area ratio of 1.02 and localization error of 0.44 mm (see Table 5.11). Therefore, for experimental testing of the system is suggested to monitor the relative permittivity change $\Delta\ \varepsilon_r$ for the temperature monitoring, as it provides a resolution of 1.06 °C, and for the proper localization to be monitored a parameter that combines the qualitative evaluation of both the relative permittivity change $\Delta\ \varepsilon_r$ and the equivalent conductivity change $\Delta\ \sigma$. Alternatively, can be studied and designed an algorithm that creates a variable that would contain the most suitable data from both parameters and be solely used for the evaluation of reconstructions.

As stated in [29], a lossless MM is impossible to be accomplished. This evaluation aimed at finding the MM liquid which would allow the system to provide significant quality and quantity of the reconstructed images in both relative permittivity and equivalent conductivity domains. The matching medium's (MM) properties proved their importance in the numerical testing of the differential MWI model, as the reconstructed image quality and proper temperature recognition, are closely dependent on how the EM power is transferred into the muscle tissue phantom. A large number of combinations between different relative permittivity and equivalent conductivity MM were tested, but not all were presented in Chapter 3. In terms of quantitative evaluation, values of MM with relative permittivity ε_r between 10 and 50 does not seem to affect the results significantly, as seen in Table 5.2 and Table 5.6, with at most a 9% quantitative error difference. When imaging just the relative permittivity a MM with high relative permittivity and low equivalent conductivity provides the best quantitative results, but on the other hand, it creates significant artefacts that are hard to mask by image processing, thus showing low qualitative results (see Figure 5.6). On top of that the high permittivity MM reduces significantly the quality and quantity results for imaging the equivalent conductivity change $\Delta\sigma$. The area ratio in that case is just 0.25 with a localization error of

9.19 mm, which is significantly worse than when using MM with lower relative permittivity (see Figure 5.7 and Table 5.7).

In case of the equivalent conductivity of MM between 0.1 and 1 (S/m), variation in the quantitative results, when imaging the conductivity domain, is not big and the results are mostly poor, with the least quantitative error from the whole study at 31.14 % as seen in Table 5.8. In Table 5.12 the MM with relative permitivty at 10 and equivalent conductivity of 1 and 0.2 are compared, where a quantitative error of just 3.4 % is calculated. On the other hand in terms of equivalent conductivity qualitative evaluation, significant differences are noticed between those same matching mediums (Table 5.11). MM with σ = 0.2 S/m, improves the sensitivity of the system from 62.78 % to 90.29 % and decreases the localization error from 1.81 mm to 0.44 mm. Another pattern that exhibited in the results is that a significant decrease of the MM's ε_r, greatly improves the quality of the imaged equivalent conductivity, while not affecting the imaged relative permittivity significantly. In Table 5.7, by reducing the MM's ε_r from 50 to 25, an increase of 46.6 % of the sensitivity value is seen. Also, the area ratio increases from 0.25 to 0.72, meaning that the size of the actual heated area is better approximated, when the matching medium has a lower relative permittivity.

Finding the proper matching medium is determined by the outputs that will be monitored. In this case the suggested values maximize the quantitative and qualitative image reconstruction results for monitoring the relative permittivity change $\Delta \varepsilon_r$ and also maximize the qualitative evaluation of the equivalent conductivity σ, however diminish its temperature resolution. From these investigations it can be concluded that the most suitable matching medium for differential Microwave imaging (MWI) temperature monitoring of the pelvic region, would have the following parameters: relative permittivity ε_r from 10 to 15 (-) and equivalent conductivity σ from 0.1 to 0.3 (S/m).

6.2 Numerical models with noise

The previous section discussed the numerical solutions with no added noise as a preliminary step in investigating the system's behaviour. Then, to further deepen that knowledge, noise was introduced to prove the reliability of the determined MM (ε_r = 10, σ = 0.2 S/m). However, additional complications were discovered after doing that, not considered in a noiseless environment.

The matching medium discussed in Chapter 6.1 has significantly low dielectric values, which limits the signal amplitude between antennas. For example, in Figure 5.13, the transmission coefficient $|S_{8,20}|$ is -100 dB, while in Figure 5.15, it is closer to -80 dB. That means these areas are more prone to be masked by the noise, as shown in Figure 5.13 when the 80 dB noise is introduced. The effect of the noise on the model with a matching medium (ε_r = 10, σ = 0.2 S/m) is most significantly seen in Figure 5.13, wherein the differential S-matrix in the region where the useful signal is located, the noise has completely distorted the transmission coefficients. Therefore, as seen in Figure 5.14, the reconstructions with noise of 90 dB or higher are predominantly unsuccessful.

Conversely, a MM with higher dielectric properties improved the inter-communication between the antennas, as more power is introduced into the phantom, improving the SNR. Even though a matching medium with lower dielectric properties performed significantly better in a noiseless environment, it cannot be implemented into a real system where significant noise is always present, especially when monitoring large areas. For further prototypes of the system is suggested to use a MM with higher dielectric properties approximating the phantom itself. For this model of the system, the MM with ε_r = 40 (-) and σ = 0.7 (S/m) has proven to handle well the introduction of 80 dB noise with a resolution of 1.55 °C and a sensitivity of 83 % in the relative permittivity reconstruction (see Table 5.13 and Table 5.15). The localization error remains under 1.5 mm, which has increased almost twice compared to the no-noise reconstruction but is still acceptable. On the other hand, the reconstructed change in the permittivity outside the heated area increased more than twice, which may cause false identification of hotspots.

The truncated singular value decomposition TSVD limit is of great importance for reconstructing data with a significant amount of noise. Theoretically, the TSVD should be kept as close to the $TSVD_{max}$, calculated by equation 5.1, because more iterations of the normalized singular values will be made, meaning more detailed data is computed.

On the other hand, in an experimental environment, the noise data is contained in the higher spectrum of the normalized singular values. Therefore, with more iterations of the singular values, the ratio of the reconstructed signal and the reconstructed noise increases exponentially in favour of the noise. The only way to influence this ratio is by increasing the normalized singular values based on the number of antennas. However, we are limited in this matter by their size. That means that with the increase of the noise levels, a lower TSVD limit must be used, as seen in the reconstruction in Figure 5.16. For data with no noise was used a TSVD of 200, which is approximately close to the $TSVD_{max}$ for 22 antennas. At 90 dB noise level, a TSVD of 80 was found to be most suitable, and for 80 dB noise level, it was taken down to 33.

The equivalent conductivity changes do not provide valuable qualitative or quantitative information about the heated phantom, as also discussed for the noiseless reconstructions in Chapter 6.1. As seen in Table 5.14, the sensitivity plummets to 12 % with 80 dB of noise and the area ratio is just 0.27 (-). A parameter like specificity, in this case, gives us false insight. That is because the identified area with a thresholding of -3 dB is so small that even though the localization error is 19.8 mm, there are almost no false positive pixels. Quantitatively at 80 dB of noise, the reconstruction of the equivalent conductivity has an 84 % relative error; therefore, no useful information about the quantity of heating is gained. The conclusion that the equivalent conductivity is not a useful dielectric parameter for reconstructing temperature changes quantitatively remains correct.

Image post-processing can be a powerful tool when dealing with data with a low SNR, such as in differential Microwave temperature monitoring. Even though it is not a direct area of focus in this paper, propositions on the matter will be discussed. In Figure 5.18 can be seen the reconstruction of Configuration 3 with MM with dielectric properties $\varepsilon r = 40$ (-), $\sigma = 0.7$ (S/m) and 80 dB noise. In subpoint (a), only a regular 3x3 convolution mask was applied (3). The images have many noise spikes in the homogenous area caused by the noise reconstruction. They can be easily filtered, as seen in (b) with the proposed Gaussian convolution kernel (see Figure 5.17) and median filtering. Median filtering has the potential to be a valuable tool for such reconstructions because of its ability to filter consistent noise while preserving the edges significantly well, as seen in both permittivity and conductivity evaluations in Figure 5.18. The ideal method of dealing with noise in post-processing is to design a convolution mask based on the noise measurement of the

particular system. However, if that cannot be done, a Gaussian convolution mask and a median filtering algorithm would be the most suitable solution.

To summarize the conclusions made in this section, the numerical testing made with the software COMSOL Multiphysics and the reconstruction algorithm DBA with TSVD have provided grounds for experimental testing of the proposed MWI system for temperature monitoring in the pelvic region. Configuration number three (Figure 4.4), with 22 UWB antennas in a single plane and a MM with the dielectric properties $\varepsilon_r = 40$, $\sigma = 0.7$ S/m, provided satisfactory results regarding the position with an accuracy of 97.6 % and the amount of heating with a resolution of 1.6 °C of the target area, in the muscle phantom in working noisy environment with a base level of noise at 80 dB. The dielectric parameter monitored in these results was the relative permittivity ε_r, which has up to ten-fold higher temperature dependency than the equivalent conductivity σ, which is why it can be imaged with significantly more precision.

6.3 Experiment

6.3.1 Antenna evaluation

The UWB antennas [21] are the most essential component of the MWI system. They must exhibit similar behaviour in receiving and transmitting signals. The 23 UWB antennas proposed in [21] were created in the first phase of preparation of the experimental setup, even though only 22 were used to have spare in case of a detected fault. The assembly was done manually, which introduced uncertainty in the measurement. Figure 5.20 plots the average reflection coefficient $|S_{11}|$ of the 23 UWB antennas in contact with distilled water. Four resonance frequencies can be distinguished for all the antennas. As the frequency increases, the impedance matching between the antenna and the environment worsens. Therefore, more power is reflected, and the standard deviation between the antennas increases significantly [21]. Since the number of antennas is too big, two graphs were used for illustrative purposes. Also, the measurement was done in two groups; therefore, it is more appropriate to separate the results, as the measurement setup and calibration were not identical. Due to that, in Figure 5.20 (a) can be seen that the resonance frequencies differentiate from the ones in (b), but for 1 GHz imaging, the magnitude of $|S_{11}|$ is similar for all antennas, as seen standard deviation illustrated by the shading. Nevertheless, to compensate for that, in the experimental setup, the antennas from both groups were interpolated between each other. In Figure 5.19 can be seen that all the individual reflection coefficients satisfy the accepted threshold of $|S_{11}| < -10$ dB, which means that they exhibit a great ability to receive and transmit signals. The UWB antennas comply with the conditions set in Chapter 4.6, thereby, are integrated into the preliminary prototype of the MWI system.

6.3.2 Muscle liquid phantom

The purpose of the muscle liquid phantom is to simulate the temperature contrast by a difference in its dielectric properties. The components used to create the muscle liquid phantoms and the target values are described in Table 4.1. However, it is challenging to establish the exact properties of the liquid muscle phantom that would follow the single-pole Cole-Cole temperature dependency. The reason is that an exothermic reaction is always present from mixing the IPA and the distilled water. Because of it, the IPA is consistently evaporated from the solution, increasing the permittivity of the solution. That creates a significant uncertainty in the measurement, as seen in Table 5.17, where the uncertainty type C for the 37 °C and 45 °C is 0.73 (-) and 0.45 (-), respectively. These values approximate the actual change in the relative permittivity $\Delta\ \varepsilon_r$ (-), which is 1.15 (-), which may lead to no contrast between the mediums. To compensate for that, the phantoms were designed with slightly exaggerated dielectric properties to ensure a detectable contrast was still established. The measured relative permittivity of the phantom at 37 °C is 55.73 (-) ± 0.73 (-), while the actual value according to the temperature dependency model is 54.21 (-). For 45 °C, the measured value is 52.754 (-) ± 0.449 (-) compared to the actual permittivity: 53.06 (-). The relative permittivity is the more significant parameter for imaging, as discussed in the previous section. Therefore, it is of the utmost importance that the liquid muscle phantoms have the proper relative permittivity values. On the other hand, the equivalent conductivity is an easy parameter to stabilize, as it is only controlled by the amount of distilled water and the added salt. The uncertainty is almost negligible, with values of 0.009 S/m and 0.004 S/m for 37 °C and 45 °C, respectively. The measured equivalent conductivity is nearly identical to the value derived from the temperature dependency model (see Table 5.17).

Another problem with the muscle liquid phantoms for this system prototype is the volume necessary. The total liquid created for the study was approximately 30 liters. The more the volume is increased, the bigger the deviation of the dielectric properties becomes because of the human error factor. Therefore, even though the values were constantly measured, the dielectric properties were never stable. It is suggested for future testing to be studied the possibility of creating agar phantoms, which would be stable and easier to operate with during the measurement.

6.3.3 Preliminary experimental reconstructions and noise floor measurement

The scattering matrices from the first experimental measurement are presented in Figure 5.23. In subpoint (a), reflection coefficients $|S_{11}|$ are around -10 dB, similar to the numerical simulations. The transmission coefficients, though, do not correspond to the simulated values. The area where the transmission coefficients in the simulations with added noise had values of -80 dB to -100 dB are completely infiltrated with noise in the range of -50 dB to -70 dB. The changes in the module, seen in subpoint (b), are entirely random, ranging from values lower than -2 dB and lower than 2 dB. That cannot be directly seen, as the colorbar scale was adjusted to a fixed range to make a comparison with the simulations with noise. These random changes in the module are completely imposed by the noise. The S-matrices from the numerical simulations with added noise of 70 dB (see Appendix B) approximate most closely the S-matrices achieved from the measurement. That means that in this preliminary experimental evaluation, the noise in the system was approximately between -70 dB and -80 dB, which is much higher than the expected -95 dB, typical for the switching matrix of the VNA, because of channel coupling. In Figure 5.13 (a), which shows the differential module S-matrix of the numerical simulations without any noise, it can be observed that the change in the module created by the scattering surface is approximately from -1.5 dB to -0.5 dB. Therefore, the noise in the system has completely masked the valuable signal. Because of that, the first reconstructions presented in Figure 5.24 are unsuccessful. A low TSVD limit of 18 was used to avoid the noise-affected data. However, in this case, no useful data is present in the normalized singular values, meaning that the DBA has reconstructed only the noise fluctuations. That can be observed in the wave-like reconstructions. On top of that, since the reconstruction algorithm is linear, it cannot handle these drastic changes, so the colorbar scale shows results in the ranges of ones and tens.

As stated in Chapter 5, the MM with dielectric properties $\varepsilon_r = 10$ and $\sigma = 0.2$ S/m was used for the measurement. The effect of the matching liquid on the SNR ratio was discovered after the preliminary experiment was performed. Therefore, the simulations with the same MM as mentioned above and additional noise (see Figure 5.13), support the conclusion that one of the main reasons for the unsuccessful reconstruction is the poor communication between the antennas. The low dielectric properties of the MM are

responsible for that, as the transmitted power is decreased. In order to have information on whether the new proposed matching liquid in the previous section is experimentally feasible and if it increases the transmission coefficients, a noise floor measurement was performed with it. On top of that, a narrower IR bandpass filter of the VNA at 10 Hz was incorporated. Ten measurements were performed, so that information about the stability of the system can also be gained. Figure 5.25 and 5.26 show the change of the transmission coefficients $|S_{ij}|$ (dB), with each measurement for the 100 Hz and 10 Hz filter. Most transmission coefficients exhibit stable behaviour with fluctuations between -1 and 1 dB. On the other hand, some significantly deviate with each measurement, for example, $|S_{6,1}|$, which spikes up to 9 decibels in the 5th measurement. This unusual behaviour is based on the system's instability, which is caused by leakage of the MM of the holders and movement of the coaxial cables. Next, the differential S-matrix was computed from the ten measurements to observe the changes in the module induced by the noise with both IR bandpass filters for the newly proposed MM (see Figure 5.27). The noise is more predominant in areas where the transmission coefficients are lower. The levels of noise (a) and (b) are significantly lower than the changes in the module caused by the heated area seen in subpoint (c). In Table 5.18 are presented the mean change in the module and the standard deviation for both of the tested filters of the VNA. The 100 Hz filter has a mean value of -0.0460 dB and a standard deviation of ± 0.2397 dB, while the 10 Hz filter has a mean a lot closer to 0 dB at -0.0085 dB, but a more significant standard deviation of ± 0.3002 dB. The 10 Hz IR bandpass filter is significantly more efficient at reducing the noise level but takes a lot longer to perform the measurement with it. Since the system is unstable, the increased measurement time causes a larger standard deviation. In any case, the values of the noise floor measurement with both tested filters of the VNA are significantly lower than the signal recorded from a simulation without noise. Therefore the, experimental reconstruction should be possible.

In conclusion, the measurement of the noise floor with the newly proposed matching medium with dielectric properties $\varepsilon_r = 40$ and $\sigma = 0.7$ S/m provided evidence that reconstructions with the currently proposed prototype of the system are possible. The following conditions and suggestions should be implemented for the experiment to be successfully carried out. First and foremost, the system must be made more stable in the following ways. The MM holders must be completely waterproof, possibly not 3-D printed and attached extremely tightly to the plexiglass cage. Also, each holder's volume

of the matching medium should be measured and equally distributed to a certain level. Secondly, the liquid is not a good choice for phantom in an extensive system because it is unstable and hard to measure in large quantities. The possibility of designing agar phantoms of tissues must be looked into, which would also allow for removing the plexiglass tank entirely from the system. Finally, the fixation and proper placement of the coaxial cables must be established, as movement and bending of the cable is another possible reason for the unstable behaviour of the system. As for the settings of the VNA, an IR bandpass filter of 10 Hz must be used after the system is ensured to be stable because the measurement time is longer. For the reconstruction, the distorted Born Approximation with a truncated singular value decomposition is sufficient. However, the TSVD limit value must be adjusted according to the noise levels to avoid reconstruction of the noise. Also, imaging the relative permittivity change provides significantly more information about the magnitude and spatial distribution of the heated area since it is more temperature dependent than the equivalent conductivity. Image post-processing tools such as a median filter or a convolution mask derived from the noise in the system should be implemented.

7 Conclusion

Differential Microwave Imaging (MWI) for monitoring the temperature changes during regional hyperthermia treatment in the pelvic region has the potential to be one of the most avaliable tools for this purpose. It is non-invasive, has potential to be cost-effective, and uses low power of non-ionizing radiation. In this Bachelor thesis the feasibility of the method was studied numerically and experimentally.

Numerical models were created in the platform COMSOL Multyphysics, and for solving the inverse scattering problem and image reconstruction, the distorted Born approximation (DBA) with truncated singular value decomposition (TSVD) was implemented. With realistic noise added in MATLAB to the numerical simulations results led to temperature resolution of 1.55 °C, accuracy of 97.64 % and a localization error of 1.4 mm. These results provided grounds that the method is feasible for an experimental trail.

The experimental setup replicated closely the numerical model. It implemented the following components: a plexiglass tank, muscle liquid phantoms, 22 UWB antennas and a vector network analyser (VNA) with a 24-port switching matrix. The preliminary reconstructions were unsuccessful but valuable data was acquired and rational conclusion on the matter were made. A clear guideline and instructions on how the antenna holders have to be modified, what matching medium should be used and how the experiment must be performed are established in the discussion of this paper. In conclusion, successful image reconstruction using experimental data from the proposed prototype should be possible.

References

[1] ISSELS, R.D., et al, 2010. Neo-Adjuvant Chemotherapy Alone Or with Regional Hyperthermia for Localised High-Risk Soft-Tissue Sarcoma: A Randomised Phase 3 Multicentre Study. *Lancet Oncology*, 06, vol. 11, no. 6, pp. 561-70 ProQuest One Academic. ISSN 14702045.

[2] C. A. Balanis, *Advanced Engineering Electromagnetics*, Solution Manual. Wiley, 1989.

[3] POZAR, David M. *Microwave engineering*. John wiley & sons, 2011.

[4] Rau, B et al. Preoperative hyperthermia combined with radiochemotherapy in locally advanced rectal cancer. Annals of Surgery. 1998. Vol. 227, no. 3p. 380–389. DOI 10.1097/00000658-199803000-00010.

[5] CANTERS, R. A. M., M. FRANCKENA, J. VAN DER ZEE and G. C. VAN RHOON. Optimizing deep hyperthermia treatments: are locations of patient pain complaints correlated with modelled SAR peak locations? *Physics in Medicine and Biology* [online]. 2011, 56(2), 439-451 [cit. 2022-05-02]. DOI: 10.1088/0031-9155/56/2/010. ISSN 0031-9155.

[6] DE TOMMASI, Francesca, et al. Temperature Monitoring in Hyperthermia Treatments of Bone Tumors: State-of-the-Art and Future Challenges. *Sensors*, 2021, 21.16: 5470.

[7] CARNOCHAN, Paul; DICKINSON, Robert J.; JOINER, Michael C. The practical use of thermocouples for temperature measurement in clinical hyperthermia. *International journal of hyperthermia*, 1986, 2.1: 1-19.

[8] RIVENS, I., et al. Treatment monitoring and thermometry for therapeutic focused ultrasound. *International journal of hyperthermia*, 2007, 23.2: 121-139.

[9] SCHENA, Emiliano, et al. Fiber optic sensors for temperature monitoring during thermal treatments: an overview. *Sensors*, 2016, 16.7: 1144.

[10] BECKER, J. A.; GREEN, C. B.; PEARSON, GLs. Properties and uses of thermistors—Thermally sensitive resistors. *Electrical Engineering*, 1946, 65.11: 711-725.

[11] CARTER, Dennis L., et al. Magnetic resonance thermometry during hyperthermia for human high-grade sarcoma. *International Journal of Radiation Oncology* Biology* Physics*, 1998, 40.4: 815-822.

[12] WYATT, Cory, et al. Hyperthermia MRI temperature measurement: Evaluation of measurement stabilisation strategies for extremity and breast tumours. *International Journal of Hyperthermia*, 2009, 25.6: 422-433.

[13] WINTER, Lukas, et al. Design and evaluation of a hybrid radiofrequency applicator for magnetic resonance imaging and RF induced hyperthermia: electromagnetic field simulations up to 14.0 Tesla and proof-of-concept at 7.0 Tesla. *PloS one*, 2013, 8.4: e61661.

[14] LÜDEMANN, Lutz, et al. Non-invasive magnetic resonance thermography during regional hyperthermia. *International Journal of Hyperthermia*, 2010, 26.3: 273-282.

[15] WINTER, Lukas, et al. Design and evaluation of a hybrid radiofrequency applicator for magnetic resonance imaging and RF induced hyperthermia: electromagnetic field simulations up to 14.0 Tesla and proof-of-concept at 7.0 Tesla. *PloS one*, 2013, 8.4: e61661.

[16] CURTO, Sergio, et al. Quantitative, multi-institutional evaluation of MR thermometry accuracy for deep-pelvic MR-hyperthermia systems operating in multi-vendor MR-systems using a new anthropomorphic phantom. *Cancers*, 2019, 11.11: 1709.

[17] LEY, Sebastian, et al. Ultra-wideband temperature dependent dielectric spectroscopy of porcine tissue and blood in the microwave frequency range. *Sensors*, 2019, 19.7: 1707.

[18] ROSSMANN, Christian; HAEMMERICH, Dieter. Review of temperature dependence of thermal properties, dielectric properties, and perfusion of biological tissues at hyperthermic and ablation temperatures. *Critical Reviews™ in Biomedical Engineering*, 2014, 42.6.

[19] MEANEY, P. M., et al. Microwave thermal imaging: Initial in vivo experience with a single heating zone. *International journal of hyperthermia*, 2003, 19.6: 617-641.

[20] HAYNES, Mark; STANG, John; MOGHADDAM, Mahta. Real-time microwave imaging of differential temperature for thermal therapy monitoring. *IEEE Transactions on Biomedical Engineering*, 2014, 61.6: 1787-1797.

[21] FISER, Ondrej, et al. UWB Bowtie Antenna for Medical Microwave Imaging Applications. *IEEE Transactions on Antennas and Propagation*, 2022.

[22] IT'IS FOUNDATION. *Tissue Properties Database V3.0.* 2015, DOI: 10.13099/VIP21000-03-0.

[23] HRUBY, Vojtech. *Antenna for Microwave Imaging Methods in Medicine*. Prague, 2019. Master's Thesis. Czech Technical University in Prague, Faculty of Electrical Engineering. Supervisor Prof. Ing. Jan Vrba, CSc

[24] PARK, Jin-Goo, Sang-Ho LEE, Ju-Suk RYU, Yi-Koan HONG, Tae-Gon KIM and Ahmed A. BUSNAINA. Interfacial and Electrokinetic Characterization of IPA Solutions Related to Semiconductor Wafer Drying and Cleaning. *Journal of The Electrochemical Society* [online]. 2006, 153(9) [cit. 2022-05-29]. DOI: 10.1149/1.2214532. ISSN 00134651

[25] DAK 4 MHz to 3 GHz, SPEAG, *Schmid & Partner Engineering AG* [online]. [cit. 2022-05-29].

[26] MEISAK, Darya, et al. Dielectric relaxation spectroscopy and synergy effects in epoxy/MWCNT/Ni@ C composites. *Nanomaterials*, 2021, 11.2: 555.

[27] MOZEROVA, Hana, et al. Monitoring regional hyperthermia via microwave imaging: a feasibility study. In: *2020 IEEE MTT-S International Microwave Biomedical Conference (IMBioC)*. IEEE, 2020. p. 1-3.

[28] NIKOLOVA, Natalia K. Microwave imaging for breast cancer. *IEEE microwave magazine*, 2011, 12.7: 78-94.

[29] LUI, Hoi-Shun; FHAGER, Andreas. On the matching medium for microwave-based medical diagnosis. *Biomedical Physics & Engineering Express*, 2018, 4.3: 035015.

[30] MALLORQUI, J.J., N. JOACHIMOWICZ, A. BROQUETAS and J.Ch. BOLOMEY. Quantitative images of large biological bodies in microwave tomography by using REFERENCES 96 numerical and real data. *Electronics Letters* [online]. 1996, 32(23), 2138-2140 [cit. 2020-03-06]. DOI: 10.1049/el:19961409. ISSN 00135194.

[31] AGUILAR, S. M., et al. Design of a microwave breast imaging array composed of dual-band miniaturized antennas. In: *2011 XXXth URSI General Assembly and Scientific Symposium*. IEEE, 2011. p. 1-4.

[32] SCAPATICCI, R., O. M. BUCCI, I. CATAPANO and L. CROCCO. Differential Microwave Imaging for Brain Stroke Followup. *International Journal of Antennas and Propagation*. 2014, 1-11. DOI: 10.1155/2014/312528. ISSN 1687-5869.

[33] *Odpadni potrubi HT* [online]. DEK a.s., 2020 [cit. 2023-05-02]. Available at: https://www.dek.cz/pobocka-kladno/produkty/vypis/15562-odpadni-potrubi-ht

[34] R&S®ZNB vector network analyzer, *Rohde & Schwarz USA, Inc.*[online] [cit. 2023-05-03]. Available at: https://www.rohde-schwarz.com/us/products/test-and-measurement/network-analyzers/rs-znb-vector-network-analyzer_63493-11648.html#image200_14148

Appendix A: Contents of the attached ZIP file and the provided CD

- F7ABBBP_503570_Ivan _Simeonov.zip
  - Reconstruction_code
    - BA_TSVD_3D.m
    - Muscle_properties3.m
  - Reconstruction_evaluation
    - qualitative_assesment_conductivity.m
    - qualitative_assesment_permitivity.m
    - Quantitative_evaluation.m
    - Noise_floor.mat
  - S_parameters
    - plot_s1p_water.m
    - stdshade.m
  - Muscle_phantoms
    - 37deg.xlsx
    - 45deg.xlsx
- CD
  - Models (COMSOL Multiphysics)
    - 12antennas_1row_homogenous.mph
    - 12antennas_1row.mph
    - 24antennas_2rows_homogenous.mph
    - 24antennas_2rows.mph
    - 22antennas_1row_homogenous.mph
    - 22antennas_1row.mph

Appendix B

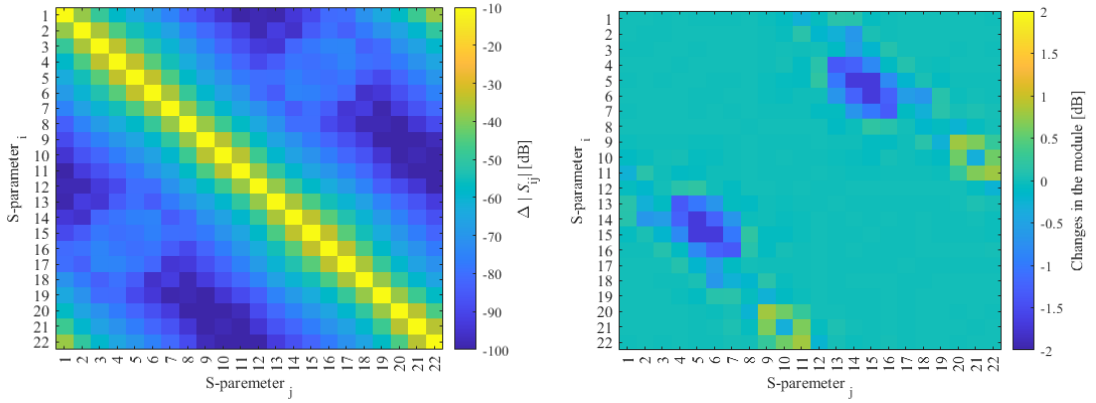

(a) No noise

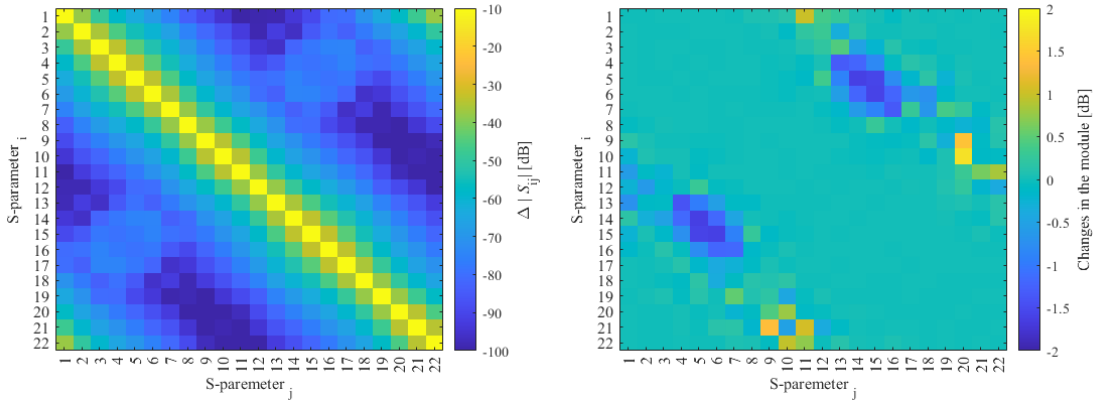

(b) 110 dB

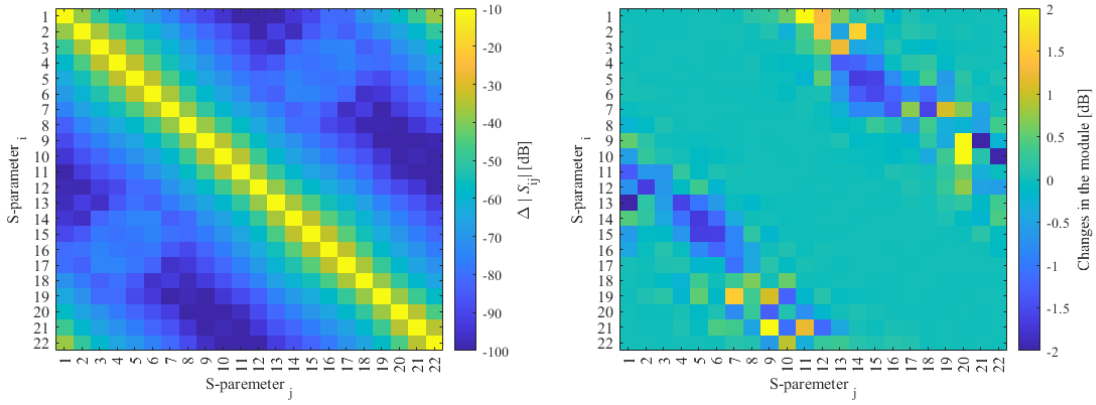

(c) 100 dB

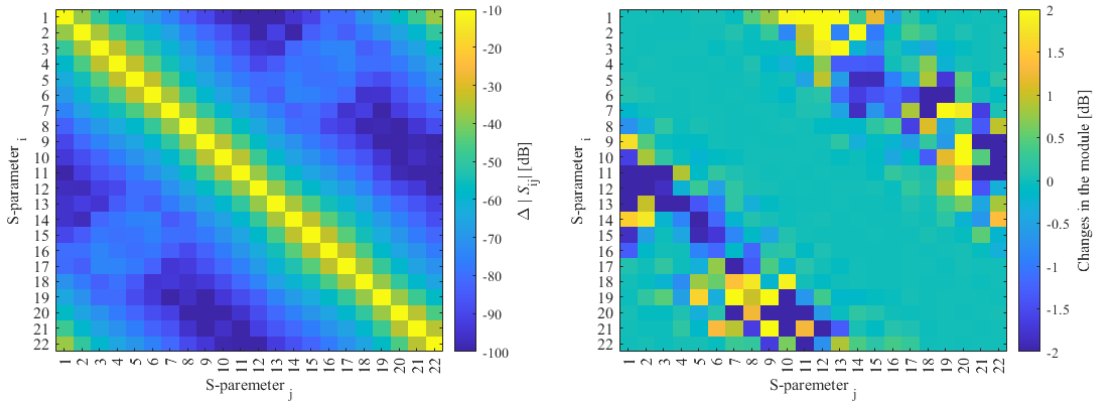

(d) 90 dB

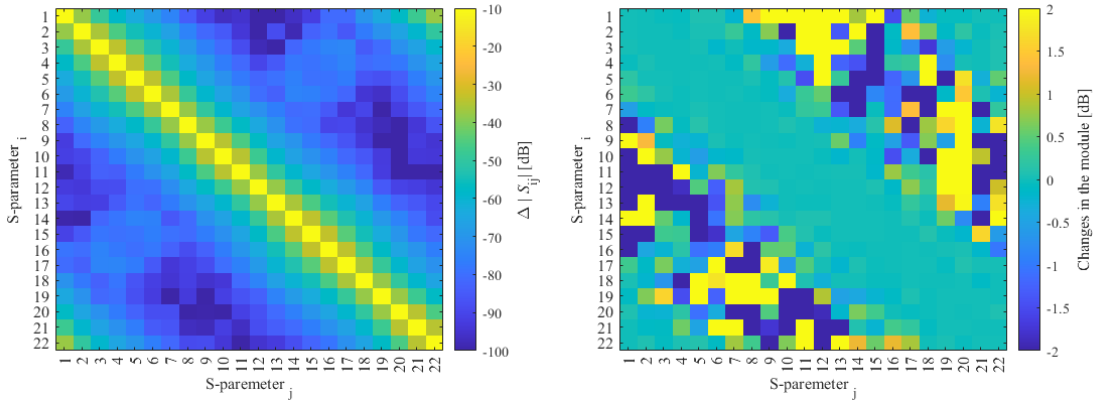

(e) 80 dB

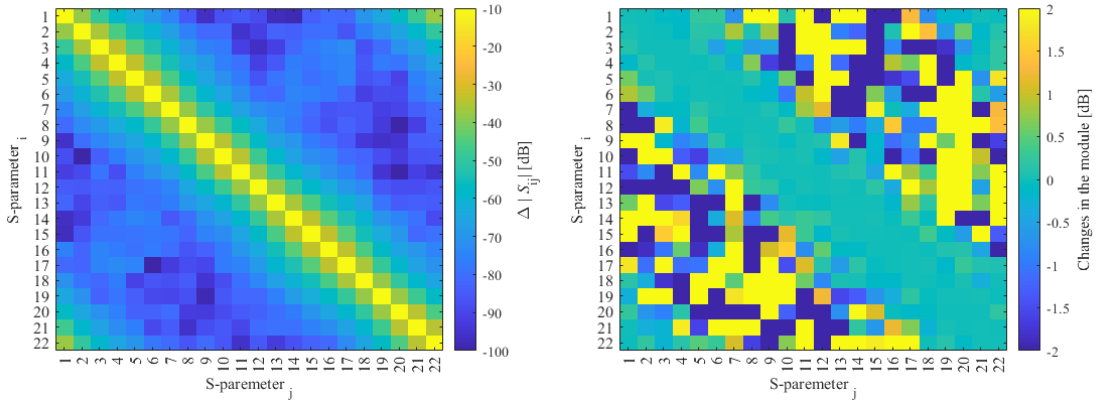

(f) 70 dB

Figure: Comparison of S-matrix and differential S-matrix for 6 levels noise of Configuration 3 numerical simulation with the following MM: ε_r = 10 (-), σ = 0.2 (S/m).

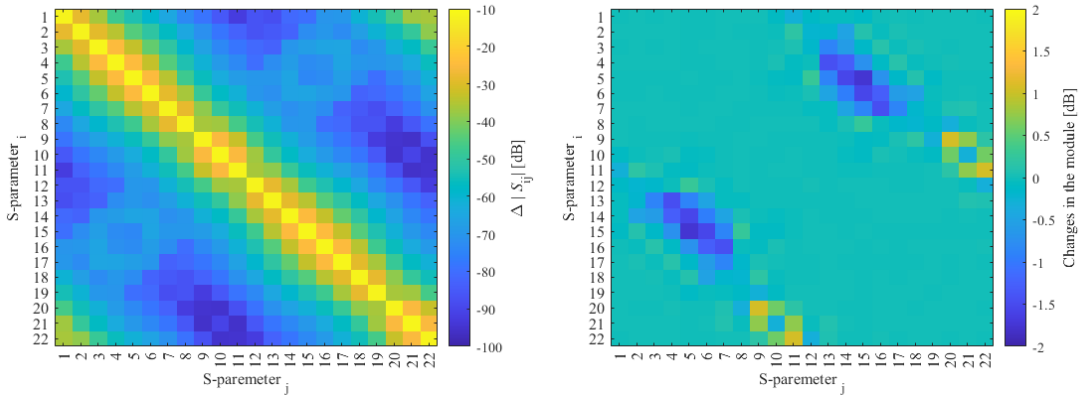

(a) No noise

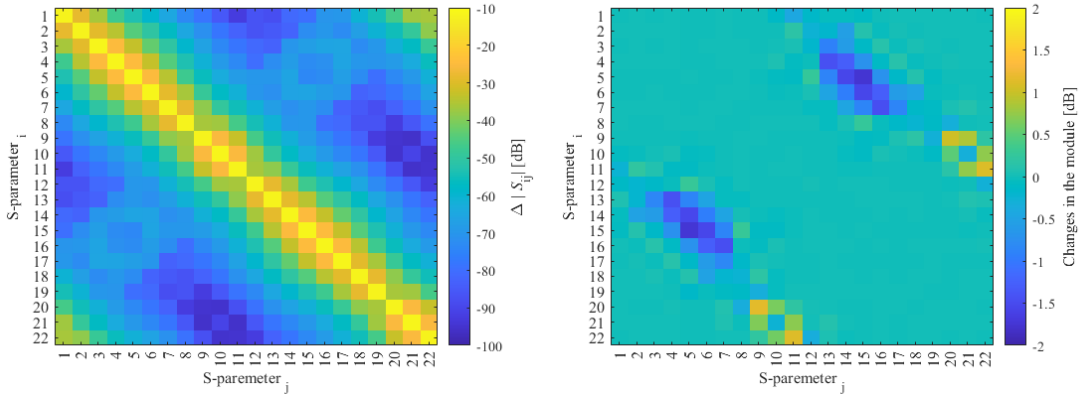

(b) 110 dB

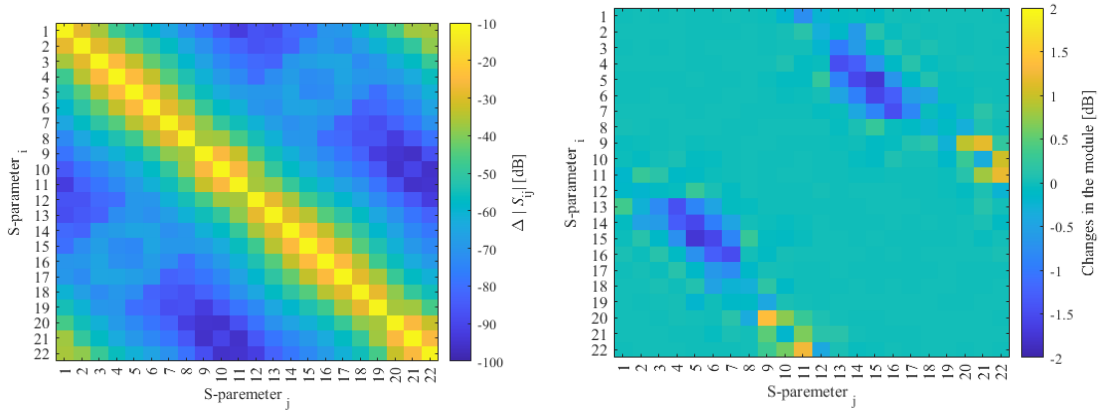

(c) 100 dB

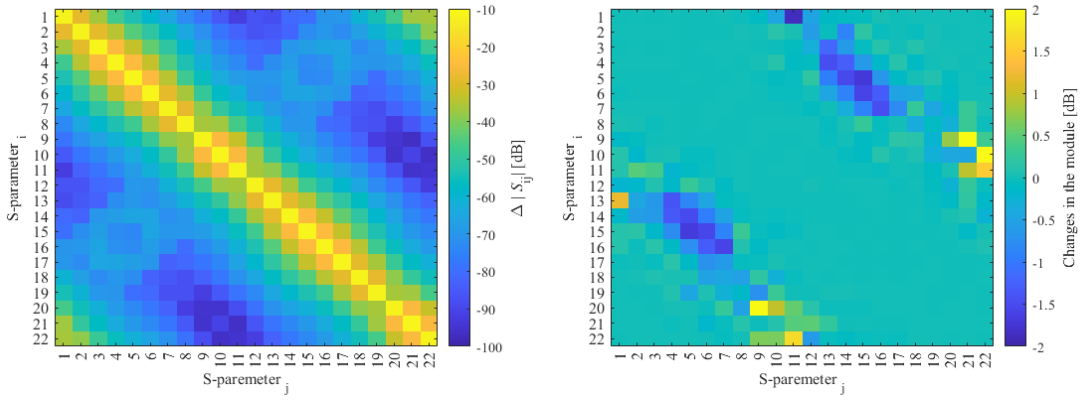

(c) 90 dB

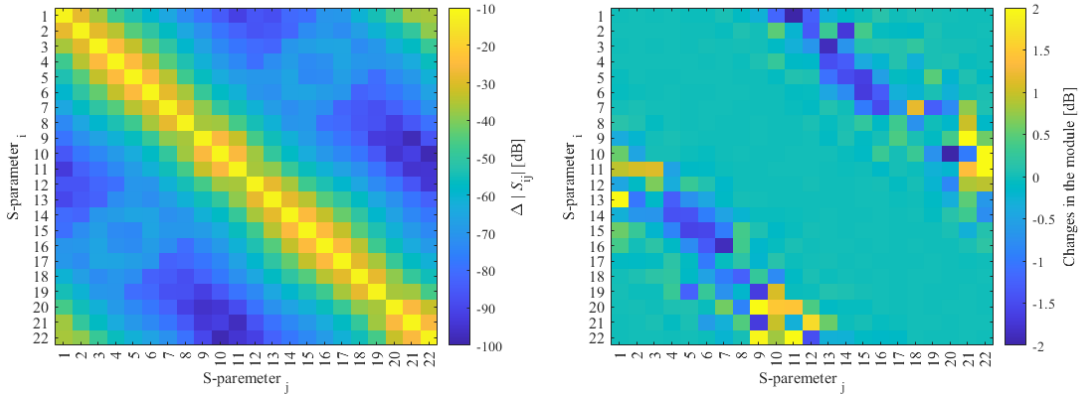

(d) 80 dB

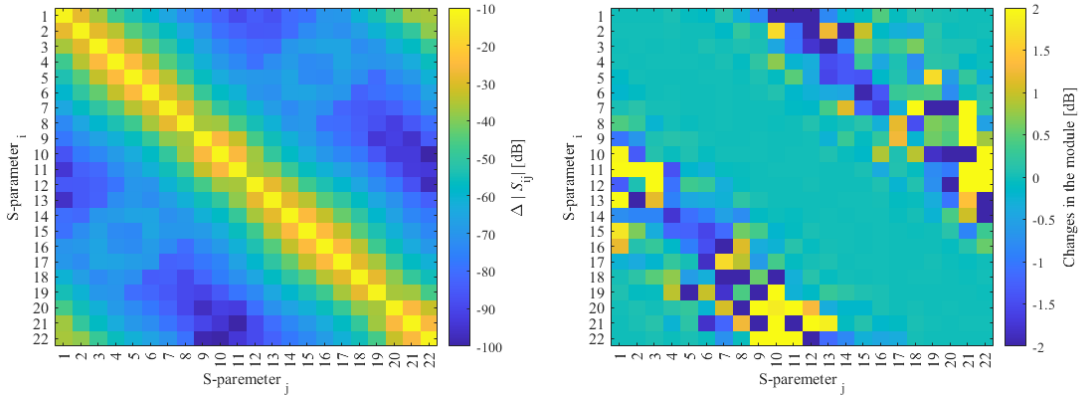

(e) 70 dB

Figure: Comparison of S-matrix and differential S-matrix for 6 levels noise of Configuration 3 numerical simulation with the following MM: $\varepsilon_r = 40$ (-), $\sigma = 0.7$ (S/m)